

Ph.D. Thesis

**Imaging mass spectrometry-based molecular histology
-Analysis of kidney and bone in Klotho-deficient mice-**

(イメージング質量分析を用いた分子組織学的解析
-Klotho 欠損マウスの腎および骨において-)

Ph.D. Applicant Yoko Fujino

Biomedical Sciences Major
Graduate School of Biomedical & Health Sciences
Hiroshima University

Supervisor: Professor Mitsugi Okada, D.D.S., Ph.D.

2015

ACKNOWLEDGEMENTS

Completion of this thesis would not have been possible without the guidance and help of several individuals who in one way or another provided me valuable assistance in the preparation and completion of this study.

First, with deep respect, I would like to express my sincere gratitude to Prof. Mitsugi Okada, Head of Special Care Dentistry, and Prof. Yuji Yoshiko, Head of Department of Calcified Tissue Biology, Hiroshima University. They taught me valuable ways of thinking and research.

Sincere gratitude is also extended to my academic advisors, Prof. Hiroki Nikawa from Department of Oral Biology & Engineering, Assistant Prof. Tomoko Minamizaki from Department of Calcified Tissue Biology, Prof. Emeritus Kazuo Tanne, and Prof. Emeritus Tetsuji Ogawa for their excellent suggestions and instructions.

My sincere gratitude also goes to the thesis committee, Prof. Takashi Takata from Department of Oral Maxillofacial Pathobiology, and Prof. Kotaro Tanimoto from Department of Orthodontics and Craniofacial Department Biology for their encouragement, insightful comments, and questions.

I also have deep appreciation for Dr. Takaaki Miyaji from Advanced Science Research Center, Okayama University, and Dr. Ikue Hayashi from Central Laboratory for their suggestions and instructions regarding proteomic analysis.

I am dearly grateful to all the members of Department of Calcified Tissue Biology, Hiroshima University, Special Care Dentistry, and Center of Oral Clinical Examination, Hiroshima University Hospital, and Advanced Science Research Center, Okayama University for their support and help to finish my study.

APPENDIX

A part of this study was presented in the following meetings:

1. Imaging Mass Spectrometry-based Molecular Histology of Bone Shows the Implication of MEPE-ASARM for the Klotho-Deficient Phenotype. The American Society for Bone and Mineral Research 2013 Annual Meeting. Baltimore, Oct. 2013.
2. Klotho 欠損マウス腎臓のイメージング質量分析. The 69th Annual Meeting of the Japanese Association of Anatomists-Bureau of Chuugoku, Shikoku. Hiroshima, Oct. 2014.
3. Imaging Mass Spectrometry-based Molecular Histology of Klotho-Deficient Mice with a Syndrome Resembling Human Premature Aging. The 31th Annual Meeting of the Japanese Society for Disability and Oral Health. Sendai, Nov. 2014.

CONTENTS

Chapter 1: Analysis of mouse renal proteins involved in *Klotho* deficiency by using MALDI imaging mass spectrometry

1. Abstract.....	1
2. Introduction.....	3
3. Material and Methods.....	5
3.1. Materials	
3.2. Animals	
3.3. Specimen preparation	
3.4. Trypsin digestion	
3.5. MALDI-IMS	
3.6. LC-MS-MS	
3.7. Immunohistochemistry	
4. Results.....	8
4.1. Comparison of MS distribution between WT and <i>kl^{-/-}</i> mouse kidneys by MALDI-IMS without trypsin digestion	
4.2. Detection and identification of proteins using a combination of MALDI-IMS and LC-MS-MS after trypsinization	
4.3. SCG1 localization at glomeruli, proximal and distal renal tubules in <i>kl^{-/-}</i> mice	
5. Discussion.....	10
6. Figure Legends.....	13
7. Figures and Tables.....	14
8. References.....	24

Chapter 2: Imaging and mapping of Klotho-deficient mouse bone using MALDI imaging mass spectrometry

1. Abstract	31
2. Introduction.....	33
3. Material and Methods.....	35
3.1. Materials	
3.2. Animals	
3.3. Specimen preparation	
3.4. Staining	
3.5. MALDI-IMS and MS-MS	
4. Results.....	37
4.1. Histological and histochemical features of bones with or without pretreatment	
4.2. Comparison of MALDI-IMS between bones with or without pretreatment	
4.3. Metabolomics with WT and <i>kl</i>^{-/-} mouse femurs	
5. Discussion.....	40
6. Figure Legends.....	43
7. Figures and Tables.....	45
8. References.....	56

CHAPTER 1

Analysis of mouse renal proteins involved in Klotho deficiency by using MALDI imaging mass spectrometry

1. Abstract

The recent development of matrix-assisted laser desorption/ionization-imaging mass spectrometry (MALDI-IMS) approaches has enabled determination of the detailed spatial distribution of molecules in frozen tissues. However, consistent detection of various species using MALDI-IMS approaches has not been achieved. Thus, this study was conducted to determine whether a combination method involving liquid chromatography (LC)-MS-MS and MALDI-IMS with trypsin digestion could be used to evaluate spatial distribution using cryosections from wild-type (WT) and Klotho knockout ($kl^{-/-}$) mouse kidneys. MALDI-IMS (m/z , mass-to-charge ratio; 1000–60,000) of frozen kidney tissues collected from 7-week-old male WT and $kl^{-/-}$ mice was used to determine genotype-specific differences of the MS distribution. Neighboring sections were subjected to MALDI-IMS (m/z 600–6000) and LC-MS-MS after trypsinization, and the distribution of molecules identified by LC-MS-MS were reflected by MALDI-IMS. As a result, titin, a very large protein (approximately 3800 kDa) was successfully detected. Sixty-one and 33 proteins were detected in only WT and $kl^{-/-}$ mouse kidneys, respectively. Among these, high mobility group protein B1, thymosin β 4, and RAD51-associated protein 1 from WT and fructose biphosphate aldolase A, chromogranin A and secretogranin-1 from $kl^{-/-}$ were originally linked to the morbid state in $kl^{-/-}$ mice. Additionally, secretogranin-1 was highly detected in the glomeruli, renal tubules, and blood vessels of $kl^{-/-}$ mouse kidneys by immunohistochemistry. These

results showed that a combination of MALDI-IMS and LC-MS-MS with trypsin digestion is useful for visualizing and identifying novel pathologic proteins in frozen tissues.

2. Introduction

Recently, omics approaches have been actively used to explore variations in whole molecules constituting an organism and analyzing life activity and pathogenesis. Anomalies in protein expression, distribution, and metabolism are frequently observed in pathological conditions; therefore, information obtained from proteomics and metabolomics studies has become particularly important for elucidating the etiology and for diagnosis. Conventional imaging techniques such as immunohistochemistry require labeling and show difficulties in discovering new pathological molecules in the tissue. Mass spectrometry (MS) is a commonly used technology for detecting analytes in proteomics and metabolomics research and can directly define individual molecular species in intricate samples, thus broadening our understanding of biological molecules; however, liquid chromatography (LC)-MS or gas chromatography (GC)-MS analyses require the use of tissue homogenates, and thus, all tissue localization information is lost.

Among the several MS ionization techniques used for direct tissue analysis, matrix-assisted laser desorption/ionization (MALDI)-MS is a powerful tool because of its wide detection range of biomolecules [1, 2]. Imaging by MALDI-MS (MALDI-IMS) reveals the detailed spatial distribution of molecules in biological samples [3]. In MALDI-IMS, however, consistent detection of species over 25 kDa has not been achieved [4]. To overcome this limitation, proteins with high molecular mass are digested by proteolytic enzymes such as trypsin, pepsin, and formic acid, and MS-MS is carried out *in situ* following protease digestion of tissue sections [5, 6]. This MS-MS approach must be performed under optimal spotting conditions for digestion and often exhibits poor digestion efficiency because of the small droplets of enzyme solution present. To overcome this limitation, digestive extraction from neighboring sections were applied liquid chromatography (LC)-MS-MS to identify the proteins present,

followed by MALDI-IMS analysis.

Aging rodents exhibit significantly lower renal α -Klotho (Klotho) protein expression than do young rodents [7]. The *klotho* gene was serendipitously identified as a gene mutated in a mouse strain (*kl/kl* mice) suffering from a syndrome resembling accelerated human aging, including atrophy of the genital organs and thymus, arteriosclerosis, ectopic calcification, and osteoporosis [8]. Klotho is a single-pass transmembrane glycoprotein that is predominantly expressed in the distal convoluted tubules, choroid plexus of the brain, and parathyroid glands [8, 9]. Klotho protein forms constitutive binary complexes with multiple fibroblast growth factor (FGF) receptors (FGFR1c, 3c, and 4), selectively increasing their affinity to FGF23 [10], which is mainly derived from osteolineage cells [11]. Klotho also acts to maintain homeostasis in phosphate and vitamin D metabolism by regulating the sodium phosphate co-transporter and vitamin D-metabolizing enzymes in the kidneys [12]. Partial deletion of Klotho in the distal tubules increases the renal protein expression of vitamin D receptor and sodium-dependent phosphate transport protein 2A [13]. Recent studies have also reported the function of circulating soluble Klotho. Soluble Klotho is generated by cleavage [14] and can act as a paracrine or endocrine mediator independently of the FGF23 pathways by promoting renal calcium reabsorption through stabilization of the transient receptor potential vanillid-5 channel in the distal tubules and by reducing serum levels of 1,25-dihydroxyvitamin D₃ [15]. These previous findings provide limited evidence for a pathogenic role of Klotho in altering the production and/or distribution of several proteins involved in aging-related disorders such as chronic kidney disease (CKD) and kidney stones.

Here, this study conducted comparative proteome analysis of sections from wild-type (WT) and Klotho knockout (*kl^{-/-}*) mouse kidneys to identify novel pathologic proteins using a combination of MALDI-IMS and LC-MS-MS.

3. Materials and Methods

3.1. Materials

Conductive indium tin oxide (ITO)-coated glass slides (100 Ω) were purchased from Matsunami Glass Ind., Ltd., (Osaka, Japan). Trypsin was purchased from Promega KK (Tokyo, Japan). Sinapic acid (SA) and α -cyano-4-hydroxycinnamic acid matrix were purchased from Bruker Daltonics (Bremen, Germany). Acetonitrile (ACN) was purchased from Merck (Darmstadt, Germany). Carboxymethylcellulose (CMC, 2%) was purchased from Leica Microsystems (Wetzlar, Germany). Trifluoroacetic acid (TFA), 2,5-dihydroxy-benzoic acid (DHB), and all other chemicals, unless otherwise specified, were purchased from Sigma–Aldrich Co. (St. Louis, MO).

3.2. Animals

Klotho heterozygous mice ($kl^{+/+}$) were purchased from CLEA, Inc. (Osaka, Japan). $kl^{-/-}$ mice were obtained by mating $kl^{+/+}$ mice. Mice were housed and handled to minimize pain or discomfort to the animals according to the protocols approved by the Institutional Animal Care and Use Committee at the Central Institute for Experimental Animals and the Committee of Animal Experimentation at Hiroshima University. Genotyping of *Klotho* knockout mice and *Klotho* WT mice was conducted as described previously [16].

3.3. Specimen preparation

Seven week-old male WT and $kl^{-/-}$ mice were euthanized and whole kidneys were extracted. For MALDI-IMS, LC-MS-MS, and immunohistochemistry, the kidneys were rapidly embedded in a stainless steel container filled with 2% CMC and then placed in dry ice-cooled hexane to form frozen CMC blocks. Each frozen block was stored at -80°C until sectioning. Tissues were sectioned (10 μm) using a CM 3050 S cryostat (Leica) and placed on the ITO-coated slides, followed by washing with 70% ethanol

and 100% ethanol and drying.

3.4. Trypsin digestion

After washing and drying of the neighboring sections (one for MALDI-IMS and another for LC-MS-MS), 200 μ L of trypsin solution (100 ng/ μ L in 40 mM ammonium bicarbonate: ACN = 9:1) was applied in an ImagePrepTM device (Bruker Daltonics) using the standard SA method and then the sections were placed in tubes under 100% relative humidity conditions at 37°C for 90 min.

3.5. MALDI-IMS

The matrix solutions composed of 10 mg/mL SA in 60% ACN (0.2% TFA) or 30 mg/mL DHB in 50% methanol (1% TFA), for trypsinized or untrypsinized sections, respectively, were evenly sprayed onto the sections using an ImagePrepTM device using the standard SA method. MALDI images were acquired using the UltrafleXtreme MALDI-TOF mass spectrometer (Bruker Daltonics) in linear positive ion mode in a range of m/z (mass-to-charge ratio) of 1000–60,000 or 600–6000 for untrypsinized or trypsinized sections, respectively. A spatial resolution of 35 μ m was used. For positioning of the glomeruli and renal tubules, neighboring sections were subjected to hematoxylin-eosin (HE) staining.

3.6. LC-MS-MS

Peptides from tryptic digests on the slides were reconstituted in 0.1% TFA, separated, and analyzed by LC-MS-MS using an EASY-nLC system (Bruker Daltonics) coupled to an ultraflextreme TOF/OTF with Smartbeam II (Bruker Daltonics). The LC system was configured with an L-column2 ODS (2 μ m, 0.2 ϕ \times 50 mm, Chemicals Evaluation and Research Institute, Tokyo, Japan) for 65 min with a gradient of solvent A (0.1% TFA in H₂O) and solvent B (ACN) at a flow rate of 0.9 μ L/min. The gradient was performed as follows; 0–3 min 95% A and 5% B, then to 50% A and 50% B at 60 min,

5% A and 95% B from 61 to 64 min, and 95% A and 5% B at 65 min. A total of 248 fractions were obtained from 3 to 65 min and subjected to MS and MS-MS analysis. MS-MS data were evaluated using the Mascot search engine (version 2.4.1, Matrix Sciences, London, UK) for protein identification. The protein list was also functionally evaluated applying UniProtKB (<http://www.uniprot.org/>).

3.7. Immunohistochemistry

For immunofluorescence staining, frozen sections (5 μm) were prepared as described above and perfused with 4% paraformaldehyde phosphate-buffered saline (PBS) for 3 min. Briefly, the sections were rinsed for 5 min with PBS, incubated in washing buffer (PBS containing 50 mM NH_4Cl) for 10 min, and incubated in blocking buffer (washing buffer containing 2% bovine serum albumin and 0.05% saponin) for 20 min. The sections were incubated with goat polyclonal anti-chromogranin B antibody (1:100, Santa Cruz Biotechnology, Inc., Santa Cruz, CA) overnight at 4°C. After 3 \times 5 min of washing with PBS, the sections were incubated in CyTM3-conjugated donkey anti-goat IgG (1:400; Jackson ImmunoResearch Lab, West Grove, PA) for 1 h at room temperature. Antibody specificity was also evaluated using blocking peptide (1:20, Santa Cruz Biotechnology). DAPI staining was also performed for counterstaining.

4. Results

4.1. Comparison of MS distribution between WT and $kl^{-/-}$ mouse kidneys by MALDI-IMS without trypsin digestion

To identify proteins showing differential distributions between genotypes, the average mass spectra of cryosections from both kidneys were compared. Among the setting measurement ranges (m/z 1000–60,000), the mass spectrum of the good S/N ratio was detected up to approximately m/z 16,000 in both genotypes (Figure 1A, B). According to MALDI-IMS, more than 30 proteins were differentially distributed between genotypes; for example, a molecule at m/z 14,978.85 was strongly detected in the WT but not in $kl^{-/-}$ mouse kidneys (Figure 1C), and a molecule at m/z 13,990.64 was strongly detected in $kl^{-/-}$ but not in WT mouse kidneys (Figure 1D).

4.2. Detection and identification of proteins using a combination of MALDI-IMS and LC-MS-MS after trypsinization

To check evaluate whether the combination method of MALDI-IMS and LC-MS-MS is useful, the cryosections were trypsinized and then subjected to MALDI-IMS (m/z 600–6000) and LC-MS-MS. The number of detectable mass spectra was increased by digestion in both genotypes in MALDI-IMS analysis (Figure 2A–D). A total of 103 and 76 proteins were identified when the sequences were aligned to LC-MS-MS spectra in the Mascot database, and of these, 97 and 69 proteins were matched to MALDI-IMS spectra in the WT and $kl^{-/-}$ mouse kidney, respectively. Sixty-one and 33 proteins were detected in only the WT and $kl^{-/-}$ mouse kidney, respectively (Table 1A, B). High mobility group protein B1 (HMGB1), thymosin β 4, RAD51-associated protein 1 (R51A1), superoxide dismutase (Table 1A), Wnt5, fructose biphosphate aldolase A, chromogranin A (CMGA), and secretogranin-1 (SCG1) (Table 1B) may contribute to renal pathology in $kl^{-/-}$ mice (see **Discussion**). Thirty-six proteins were detected in both genotypes (Table 1C). Among the identified proteins, titin was the largest

(approximately 3900 kDa, Table 1A).

Based on functional classification, nucleic acid binding proteins were the most frequently detected (42% in WT and 37% in *kl^{-/-}*), followed by enzymes (20% in WT and 28% in *kl^{-/-}*) (Figure 3). Membrane proteins and secretory proteins were also observed, and the number different protein types did not show a marked difference between genotypes.

4.3. SCG1 localization at glomeruli, proximal and distal renal tubules in *kl^{-/-}* mice

To compare the localization in detail, the irradiation ranges were set to the glomeruli and proximal and distal renal tubules referring to the neighboring sections stained with HE (Figure 4A). In WT mice, 8, 9, and 3 proteins were detected in the glomeruli and the proximal and distal renal tubules, respectively (Table 2A). Of these, 5 proteins including R51A1 were observed in only WT. However, in *kl^{-/-}* mice, 21 proteins were detected in each area, and 11 proteins including ALDOA, CMGA, and SCG1 were observed in only *kl^{-/-}* mice (Table 2B). Based on MALDI-IMS, *m/z* 1269.629 was identified as one of the fragments of SCG1 by LC-MS-MS in the glomeruli and the proximal and distal renal tubules (Table 3 and Figure 4A–C).

To confirm the identification and distribution of SCG1 in the *kl^{-/-}* mouse kidney, immunohistochemistry for SCG1 was performed. Compared to WT, SCG1 immunoreactivity was strong in the glomeruli and the proximal and distal renal tubules as well as in the blood vessels in *kl^{-/-}* mice (Figure 5A–D). These results support those obtained from the combination of MALDI-IMS and LC-MS-MS.

5. Discussion

Previous studies have found changes in the expression of genes and proteins in klotho-deficient mice; however, the results were complex and clarifying the pathological mechanisms of kidney diseases in these mice is difficult. Olauson et al. (2012) showed that targeted deletion of Klotho in the kidney resulted in abundant expression of sodium-dependent phosphate transport protein 2A without tubular calcification on renal histology. Yoshida et al. (2002) demonstrated that the levels of vitamin D receptor mRNA and protein were slightly and significantly reduced, respectively, in *kl^{-/-}* mouse kidneys, which is not in accordance with previous studies even with high serum levels of 1,25-dihydroxyvitamin D₃ [13, 17-20]. This study comprehensively determined the proteomics of the *kl^{-/-}* mouse kidney to identify novel pathologic factors with localization information using a combination of MALDI-IMS and LC-MS-MS.

In this study 61 presumptive proteins were detectable in the WT mouse kidney but not in the *kl^{-/-}* mouse kidney. HMGB1, a member of the high mobility group nuclear protein family, has the capacity to produce specific changes in the structure of target DNA; it is localized in the nucleus where it exerts transcriptional activities [21-23]. HMGB1 also acts as a paracrine/autocrine factor to control cell differentiation, proliferation, and disease pathogenesis [24]. Studies using a neutralizing antibody to HMGB1 demonstrated that HMGB1 is an early mediator of injury and inflammation in the liver or kidney following ischemia-reperfusion [25, 26]. Thymosin β 4, isolated originally from the calf thymus [27] and further detected in several organs, including the kidney [28], promotes the migration of endothelial cells, angiogenesis, and tumor metastasis *in vitro* and *in vivo* [29-32]. Previous studies using MALDI-IMS indicated that thymosin β 4 was detected in colon carcinoma and pancreatic cancer [33, 34]. R51A1 is critically important for homologous recombination by interacting with both the RAD51 and

DMC1 recombinases in mitotic and meiotic cells [35-37]. R51A1 knockdown in human cells by RNA interference led to increased levels of genomic instability and decreased levels of DNA repair that decreased with age [37, 38] and RAD51 diminishes with age in kidney [39]. This study is the first to demonstrate that undetectable proteins, including HMGB1, thymosin β 4, and R51A1, in the *kl^{-/-}* mouse kidney may be related to syndromes resembling the acceleration of human aging in Klotho-deficient mice. Superoxide dismutase (SOD) is an anti-oxidant enzyme known to be associated with aging. Previous studies have found that Klotho increases the resistance to oxidative stress by upregulating the activity of a human SOD2 gene promoter [40] and that aged rats showed glomerulosclerosis and tubulointerstitial fibrosis with a significant decrease in both Klotho and mitochondrial SOD protein expression in the renal cortex [41, 42] and medulla [42]. These studies support our results showing that SOD is undetectable in the *kl^{-/-}* mouse kidney.

In contrast, 33 presumptive proteins were detectable in the *kl^{-/-}* mouse kidney but not in WT mice. Among the Wnt family that controls a variety of processes such as cell fate specification, cell migration, and cell polarity [43], most members are upregulated during renal fibrosis [44]. The soluble form of Klotho inhibits Wnt signaling and immunoprecipitates with a number of Wnt isoforms, including Wnt5a [45]. Fructose bisphosphate aldolase A (ALDOA) is a key enzyme in glycolysis and contributes to various cellular functions and biological processes [46-48]. Based on evidence that ALDOA activates the Wnt signaling pathway in a GSK-3 β -dependent manner [49], Klotho deficiency may contribute to renal pathological anomalies with ALDOA-involved Wnt signaling. CMGA and SCG1 (also known as chromogranin B) are the members of the granin family (secretogranins/chromogranins) that play an important role in the packaging and sorting of secretory products such as peptide hormones and neuropeptide in the trans-Golgi network [50]. Both CMGA and SCG1 are present in many normal (e.g., adrenal medulla and paraganglion) and neoplastic (e.g.,

pheochromocytomas and prolactinomas) tissues in the diffuse neuroendocrine system [51]. In addition to the important roles of CMGA and SCG1 as biomarkers for screening of neuroendocrine tumors [52, 53], previous studies have shown that CMGA levels in the serum were elevated in various disorders, including renal failure [54-56]. Cleavage of CMGA by thrombin inhibits angiogenesis *in vitro* and *in vivo* [57] and angiogenesis does not function in CKD [58]; thus, CMGA may be involved in the loss of the rich peritubular capillary network in CKD. Compared to CMGA, the physiological functions of SCG1 are not well known; however, angiotensin II, which has been implicated in the pathogenesis of various glomerular diseases [59, 60], increases rat cardiomyocyte *Scg1* mRNA expression [61]. The detected proteins, Wnt5, ALDOA, CMGA, and SCG1, in the *kt^{-/-}* mouse kidney may contribute to pathogenesis, and further studies are needed to evaluate the effects of these proteins in *kt^{-/-}* mice.

Proteomics by MALDI-MS enables the identification of pathological factors without labeling, but the size of proteins that can be detected without digestion or optimization of conditions is limited (<25 kDa) (see **Introduction**). In this study, using a combination of MALDI-IMS and LC-MS-MS after trypsinization, the number of MS peaks was increased and the extent of localization and immunohistochemistry was stable. Furthermore, titin, which is the largest protein in vertebrate striated muscles (approximately 3900 kDa) [62], was successfully detected. This method was also successfully used to identify novel pathological proteins. The MALDI-IMS method exhibits some limitations in the quantitative and qualitative analysis and should be further improved in future studies.

6. Figure Legends

Figure 1. Comparison of MS distribution between WT and *kl^{-/-}* mouse kidney by MALDI-IMS. Average mass spectra ($m/z < 20,000$) of cryosections from WT (**A**) and *kl^{-/-}* (**B**) mouse kidney. The x-axis and the y-axis represent m/z and intensity, respectively. (**C**, **D**) The left and right images indicate WT and *kl^{-/-}* mouse kidney, respectively. (**C**) Red spots indicate the molecule of m/z 14,978.85. (**D**) Green spots show the molecule of m/z 13,990.64.

Figure 2. Comparison of average mass spectra between WT and *kl^{-/-}* mouse kidney with or without trypsinization by MALDI-IMS. Average mass spectra (m/z 600–6000) of cryosections from WT (**A**, **C**) and *kl^{-/-}* (**B**, **D**) mouse kidney with (**C**, **D**) or without (**A**, **B**) trypsin digestion.

Figure 3. Functional classification of detected proteins. Identified proteins by the combination of MALDI-IMS and LC-MS-MS in WT (**A**) and *kl^{-/-}* (**B**) were classified using UniProtKB.

Figure 4. Distribution of a fragment of SCG1 in *kl^{-/-}* mouse kidney by using a combination of MALDI-IMS and LC-MS-MS. (**A**) HE staining using the neighboring section. Blue, green, and yellow circles indicate glomeruli and proximal and distal renal tubules, respectively. (**B**) MALDI-IMS of m/z 1269.629. (**C**) Merged image of (**A**) and (**B**).

Figure 5. Immunohistochemistry for SCG1 in WT and *kl^{-/-}* mouse kidney. Immunofluorescence staining of SCG1 (**A**, **C**) and DAPI staining (**B**, **D**) in WT (**A**, **B**) and *kl^{-/-}* (**C**, **D**) mouse kidney.

Figure 1

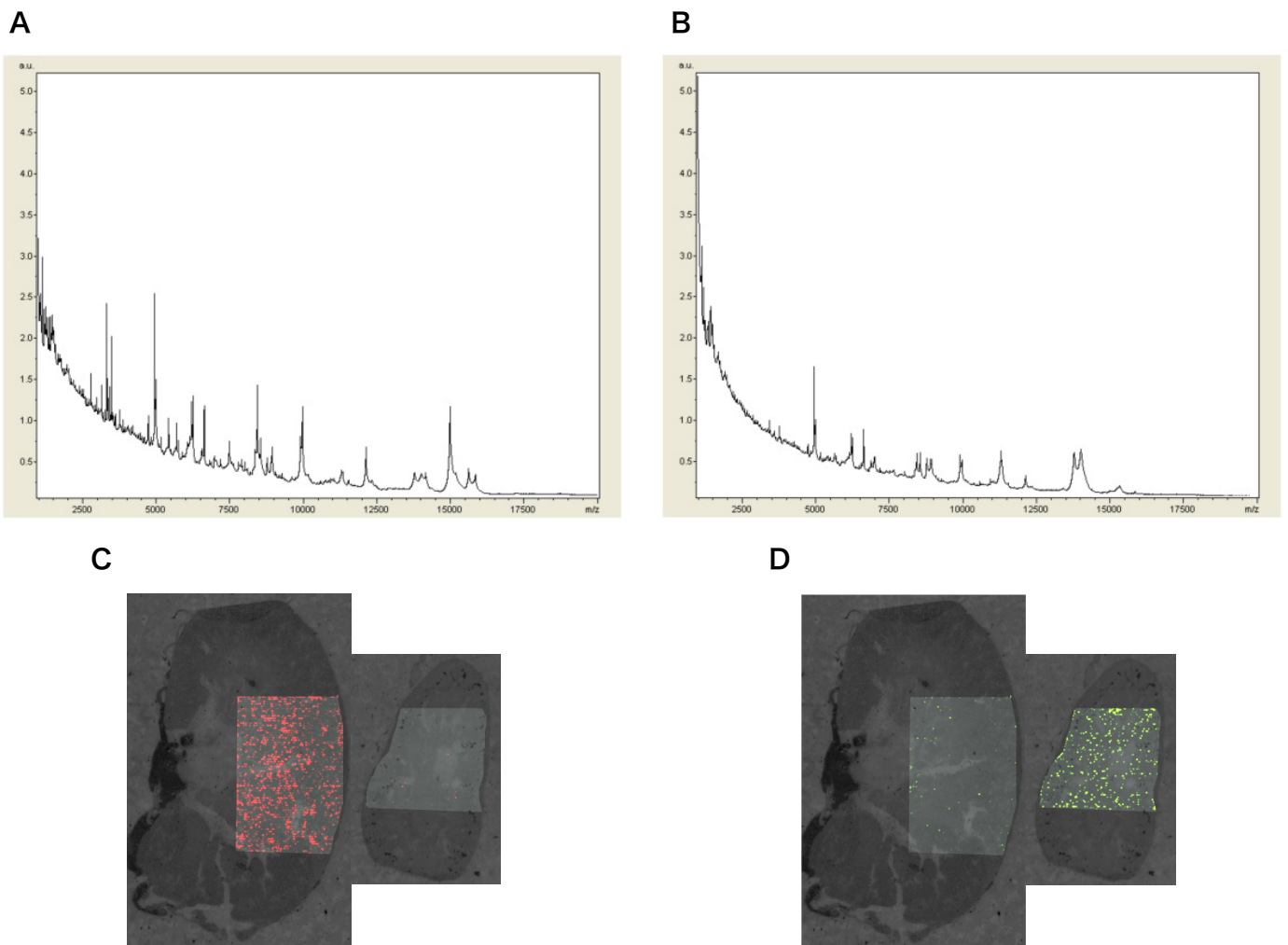
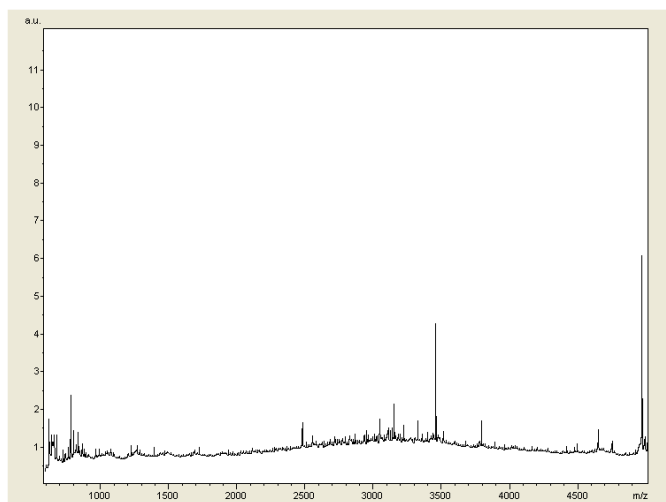
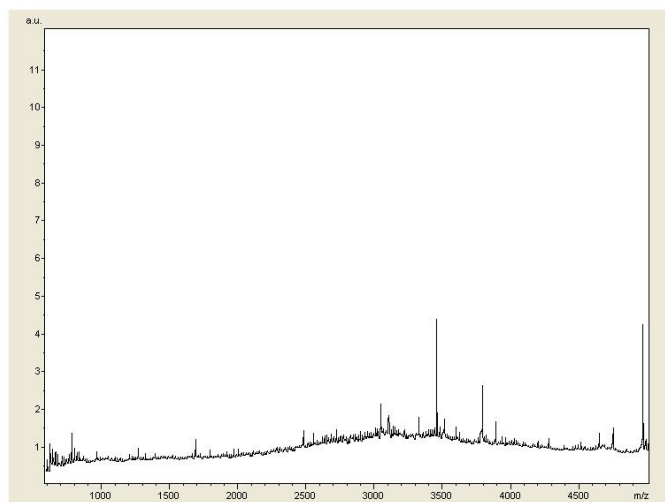


Figure 2

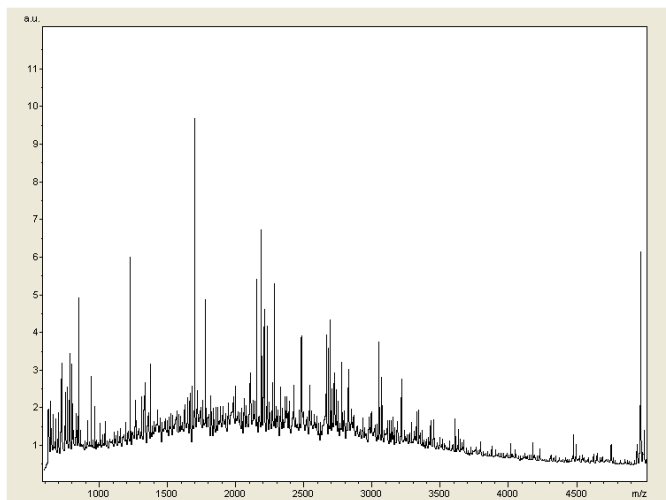
A



B



C



D

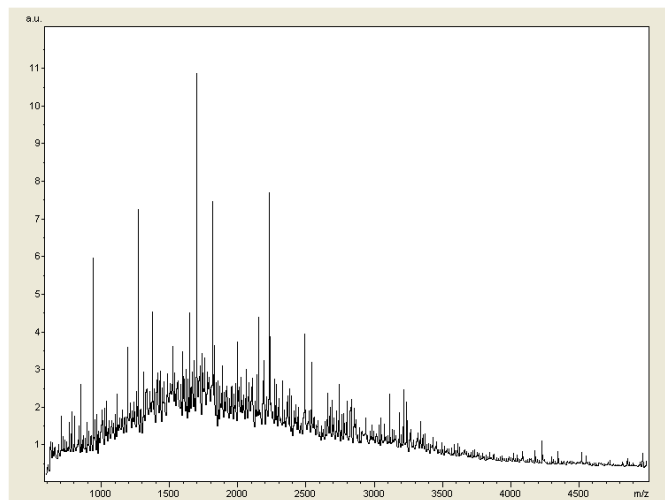


Figure 3

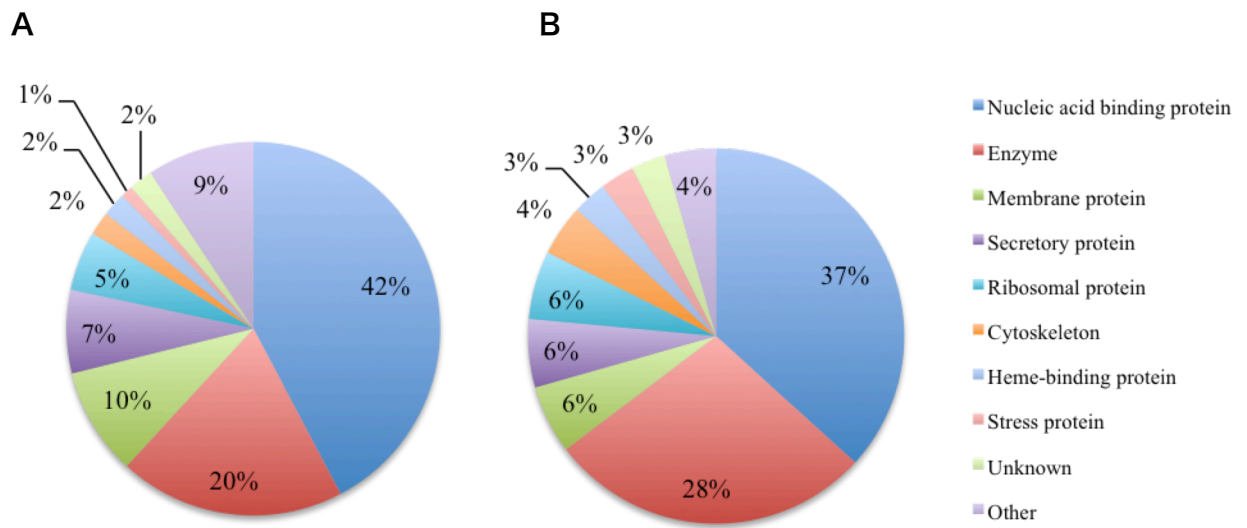


Figure 4

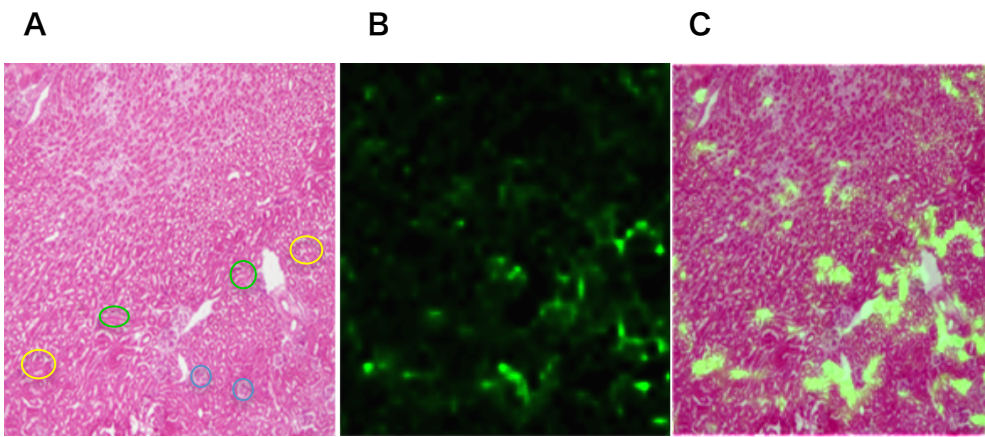


Figure 5

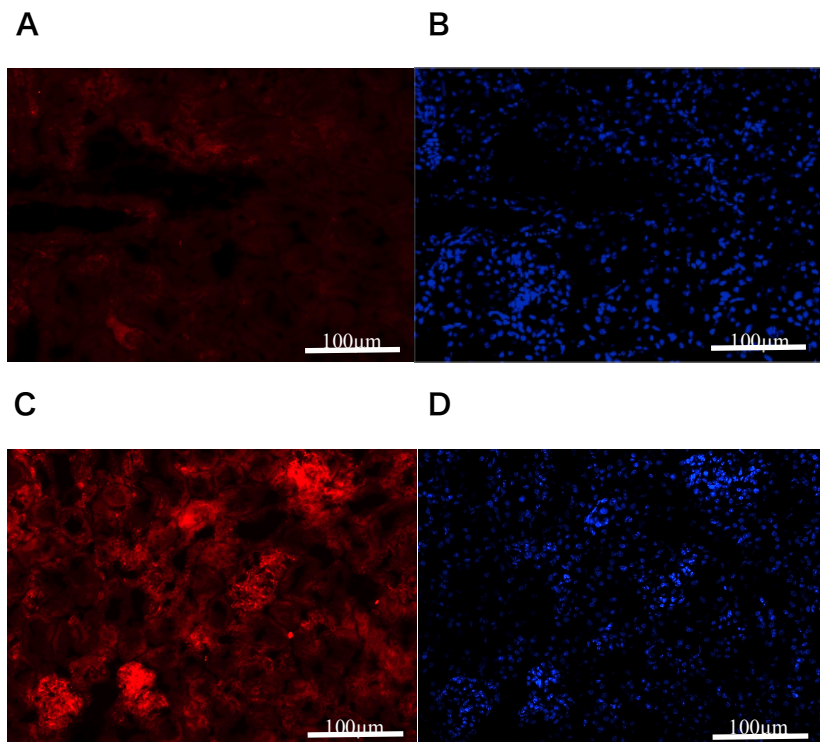


Table 1. List of proteins identified by a combination of MALDI-IMS and LC-MS-MS

A

Short name	Molecular weight	Protein name
ABCD2	83400	ATP-binding cassette sub-family D member 2
ACTB	41710	Actin, cytoplasmic 1
AFAP1	8900	Actin filament-associated protein 1
AMPL	56106	Cytosol aminopeptidase
ARFG2	56600	ADP-ribosylation factor GTPase-activating protein 2
ATIF1	12151	ATPase inhibitor, mitochondrial
ATP5J	12489	ATP synthase-coupling factor 6, mitochondrial
CC067	75100	Uncharacterized protein C3orf67 homolog
CLAP2	140700	CLIP-associating protein 2
COOA1	175600	Collagen alpha-1(XXIV) chain
DAP1	11148	Death-associated protein 1
DHX15	90900	Pre-mRNA-splicing factor ATP-dependent RNA helicase DHX15
DRG2	40692	Developmentally-regulated GTP-binding protein 2
E41L2	109873	Band 4.1-like protein 2
EF1A2	50400	Elongation factor 1-alpha 2
EIF3A	161800	Eukaryotic translation initiation factor 3 subunit A
ENOA	47111	Alpha-enolase
GDIR1	23393	Rho GDP-dissociation inhibitor 1
GRP75	73416	Stress-70 protein, mitochondrial
H10	20848	Histone H1.0
H14	21964	Histone H1.4
H15	22562	Histone H1.5
H2AV	13500	Histone H2A.V
H2B2B	13912	Histone H2B type 2-B
HDGF	26253	Hepatoma-derived growth factor
HMGA1	11607	High mobility group protein HMG-I/HMG-Y
HMGB1	24878	High mobility group protein B1
HMGN3	10763	High mobility group nucleosome-binding domain-containing protein 3
IF4B	68799	Eukaryotic translation initiation factor 4B
INO80	176410	DNA helicase INO80
K6PF	85200	6-phosphofructokinase, muscle type
K6PL	85305	6-phosphofructokinase, liver type
KHDR1	48300	KH domain-containing, RNA-binding, signal transduction-associated protein 1
KIF19	111500	Kinesin-like protein KIF19
LAP2B	50300	Lamina-associated polypeptide 2, isoforms beta/delta/epsilon/gamma
LASP1	29975	LIM and SH3 domain protein 1
MSGN1	20500	Mesogenin-1
MYEF2	63254	Myelin expression factor 2
MYLK	212792	Myosin light chain kinase, smooth muscle
NOP2	86699	Putative ribosomal RNA methyltransferase
PKNX1	47509	Homeobox protein PKNOX1
PLEC	533900	Plectin
PPIA	17960	Peptidyl-prolyl cis-trans isomerase A
PPR1B	21767	Protein phosphatase 1 regulatory subunit 1B
PTMA	12247	Prothymosin alpha
R51A1	36200	RAD51-associated protein 1
RHG32	229576	Rho GTPase-activating protein 32
RIMS2	172800	Regulating synaptic membrane exocytosis protein 2
RL14	23549	60s ribosomal protein L14
RS19	16100	40s ribosomal protein S19
RL29	17576	60S ribosomal protein L29
RMXL1	42136	RNA binding motif protein, X-linked-like-1
RS30	6644	40s ribosomal protein S30
SC6A3	68760	Sodium-dependent dopamine transporter
SODC	15933	Superoxide dismutase [Cu-Zn]
SPR1	68400	Protein spire homolog 1
SYSC	58352	Serine--tRNA ligase, cytoplasmic
TITIN	3904100	Titin
TUT7	168996	Terminal uridylyltransferase 7
TYB4	5676	Thymosin beta-4
VPS35	91700	Vacuolar protein sorting-associated protein 35

Table 1 (continued)**B**

<u>Short name</u>	<u>Molecular weight</u>	<u>Protein name</u>
AIAG1	23880	Alpha-1-acid glycoprotein 1
ACADM	46452	Medium-chain specific acyl-CoA dehydrogenase, mitochondrial
ACADS	44861	Short-chain specific acyl-CoA dehydrogenase, mitochondrial
ACOC	98063	Cytoplasmic aconitate hydratase
ACSM1	64700	Acyl-coenzyme A synthetase ACSM1, mitochondrial
ACTG	41800	Actin, cytoplasmic 2
ALDOA	39331	Fructose-bisphosphate aldolase
ALDOB	39482	Fructose-bisphosphate aldolase B
ASSY	46555	Argininosuccinate synthase
AT1A1	112910	Sodium/potassium-transporting ATPase subunit alpha-1
ATPB	56265	ATP synthase subunit beta,mit
CH60	60917	60 kDa heat shock protein, mitochondrial
CMGA	51758	Chromogranin-A
CNTRL	268700	Centriolin
EFTU	49477	Elongation factor Tu, mitochondrial
H2A2A	14100	HistoneH2A type 2-A
HINT2	17300	Histidine triad nucleotide-binding protein 2, mitochondrial
HNRPU	87863	Heterogeneous nuclear ribonucl
IKZF5	46400	Zinc finger protein Pegasus
KAD2	26452	Adenylate kinase 2, mitochondrial
LDHB	36549	L-lactate dehydrogenase B chai
LRP11	51800	Prolow-density lipoprotein receptor-related protein 1
NDRG1	42981	Protein NDRG1
PIN4	13806	Peptidyl-prolyl cis-trans isomerase NIMA-interacting 4
PRS6B	47379	26S protease regulatory subuni
PURB	33881	Transcriptional activator protein Pur-beta
RL6	33489	60S ribosomal protein L6
SC61B	9952	Protein transport protein Sec61 subunit beta
SCG1	77922	Secretogranin-1
TAGL2	22400	Transgelin-2
TMCO3	75854	Transmembrane and coiled-coil domain-containing protein 3
VIME	53655	Vimentin
WNT5A	42300	Protein Wnt-5a

Table 1 (continued)**C**

Short name	Molecular weight	Protein name
ACON	85410	Aconitate hydratase, mitochondrial
AL4A1	61802	Delta-1-pyrroline-5-carboxylate dehydrogenase, mitochondrial
CATA	59758	Catalase
EF1A1	50082	Elongation factor 1-alpha 1
ETFB	27606	Electron transfer flavoprotein subunit beta
EZRI	69364	Ezrin
FIBB	54718	Fibrinogen beta chain
G3P	35787	Glyceraldehyde-3-phosphate dehydrogenase
H12	21254	Histone H1.2
H13	22086	Histone H1.3
H2A1H	13942	HistoneH2A type 1-H
H2B1B	13944	Histone H2B type 1-B
H2B1H	13912	Histone H2B type 1-H
H31	15394	Histone H3.1
H4	11360	Histone H4
HBA	15076	Hemoglobin subunit alpha
HBB1	15830	Hemoglobin subunit beta-1
HMGN2	9417	Non-histone chromosomal protein HMG-17
HNRPC	34364	Heterogeneous nuclear ribonucleoproteins C1/C21
HNRPK	50944	Heterogeneous nuclear ribonucleoprotein K
LRMP	59551	Lymphoid-restricted membrane protein
MDHM	35589	Malate dehydrogenase, mitochondrial
NID1	136450	Nidogen-1
NPM	32540	Nucleophosmin
PTMS	11423	Parathyrosin
RL24	17768	60S ribosomal protein L24
ROA1	34175	Heterogeneous nuclear ribonucleoprotein A1
ROA2	37380	Heterogeneous nuclear ribonucleoproteins A2/B1
ROA3	39628	Heterogeneous nuclear ribonucleoprotein A3
ROBO2	161090	Roundabout homolog 2
RRBP1	172776	Ribosome-binding protein 1
RS10	18904	40S ribosomal protein S10
SFPQ	75394	Splicing factor, proline and
THIL	44787	Acetyl-CoA acetyltransferase
THOC4	26900	THO complex subunit 4
YBOX1	35709	Nuclease-sensitive element-binding protein 1

Table 2. List of proteins identified from glomeruli, proximal, and distal renal tubules

A			B		
glomerulus	proximal renal tubule	distal renal tubule	glomeruli	proximal renal tubules	distal renal tubules
COOA1 *	COOA1 *	COOA1 *	ACON	ACON	ACON
ENOA *	ENOA *	ENOA *	ACTG *	ACTG *	ACTG *
H2A1H	H2A1H	VPS35 *	AL4A1	AL4A1	AL4A1
H4	H4		ALDOA *	ALDOA *	ALDOA *
HBA	HBA		Assy *	EF1A1	ATPB *
INO80 *	INO80 *		CMGA *	ETFB	EF1A1
ROA2	R51A1 *		G3P	G3P	ETFB
VPS35 *	ROA2		H2A1H	H2A1H	G3P
	VPS35 *		H2A2A *	H2A2A *	H2A1H
			H31	H31	H2A2A *
			H4 *	HBA	H31
			HBA	HBB1	H4 *
			HBB1	HNRPU *	HBA
			LDHB *	LDHB *	HBB1
			PRS6B *	PRS6B *	LDHB *
			ROA2	PTMS	PRS6B *
			RRBP1	ROA2	ROA2
			RS10	RRBP1	RS10
			SCG1 *	RS10	SCG1 *
			SFPQ	SCG1 *	SFPQ
			THIL	THIL	THIL

* : the protein detected only in WT or *kl*^{-/-}

n = 2 ~ 5

Table 3. List of fragments of SCG1

<u>Protein name</u>	<u>Peptide</u>	<u><i>m/z</i></u>
Secretogranin 1	IYHSEER	933.4425 Da ± 0.6 Da
Secretogranin 1	SHHLAHR	1020.512 Da ± 0.6 Da
Secretogranin 1	SYRGLQYR	1042.543 Da ± 0.6 Da
Secretogranin 1	GRGSEEDRAPRPR	1562.718 Da ± 0.6 Da
Secretogranin 1	GSEEDRAPRPR	1269.629 Da ± 0.6 Da

8. References

1. Svatos A: Mass spectrometric imaging of small molecules. *Trends in Biotechnology* 2010, 28 (8): 425-434.
2. Yates JR, 3rd: Mass spectrometry and the age of the proteome. *Journal of Mass Spectrometry* 1998, 33 (1): 1-19.
3. Zaima N, Hayasaka T, Goto-Inoue N, Setou M: Imaging of Metabolites by MALDI Mass Spectrometry. *Journal of Oleo Science* 2009, 58 (8): 415-419.
4. Maier SK, Hahne H, Gholami AM, Balluff B, Meding S, Schoene C, Walch AK, Kuster B: Comprehensive Identification of Proteins from MALDI Imaging. *Molecular & Cellular Proteomics* 2013, 12 (10): 2901-2910.
5. Groseclose MR, Andersson M, Hardesty WM, Caprioli RM: Identification of proteins directly from tissue: *in situ* tryptic digestions coupled with imaging mass spectrometry. *Journal of Mass Spectrometry* 2007, 42 (2): 254-262.
6. Yao I, Sugiura Y, Matsumoto M, Setou M: *In situ* proteomics with imaging mass spectrometry and principal component analysis in the *Scrapper*-knockout mouse brain. *Proteomics* 2008, 8 (18): 3692-3701.
7. Manya H, Akasaka-Manya K, Endo T: Klotho protein deficiency and aging. *Geriatrics & Gerontology International* 2010, 10 Suppl 1: S80-87.
8. Kuro-o M, Matsumura Y, Aizawa H, Kawaguchi H, Suga T, Utsugi T, Ohyama Y, Kurabayashi M, Kaname T, Kume E *et al*: Mutation of the mouse *klotho* gene leads to a syndrome resembling ageing. *Nature* 1997, 390 (6655): 45-51.
9. Ben-Dov IZ, Galitzer H, Lavi-Moshayoff V, Goetz R, Kuro-o M, Mohammadi M, Sirkis R, Naveh-Many T, Silver J: The parathyroid is a target organ for FGF23 in rats. *The Journal of Clinical Investigation* 2007, 117 (12): 4003-4008.
10. Kurosu H, Ogawa Y, Miyoshi M, Yamamoto M, Nandi A, Rosenblatt KP, Baum MG, Schiavi S, Hu MC, Moe OW *et al*: Regulation of Fibroblast Growth Factor-23 Signaling by Klotho. *The Journal of Biological Chemistry* 2006, 281 (10): 6120-6123.
11. Yoshiko Y, Wang H, Minamizaki T, Ijuin C, Yamamoto R, Suemune S, Kozai K, Tanne K, Aubin JE, Maeda N: Mineralized tissue cells are a principal source

- of FGF23. *Bone* 2007, 40 (6): 1565-1573.
12. Shimada T, Hasegawa H, Yamazaki Y, Muto T, Hino R, Takeuchi Y, Fujita T, Nakahara K, Fukumoto S, Yamashita T: FGF-23 Is a Potent Regulator of Vitamin D Metabolism and Phosphate Homeostasis. *Journal of Bone and Mineral Research* 2004, 19 (3): 429-435.
 13. Olauson H, Lindberg K, Amin R, Jia T, Wernerson A, Andersson G, Larsson TE: Targeted Deletion of Klotho in Kidney Distal Tubule Disrupts Mineral Metabolism. *Journal of the American Society of Nephrology* 2012, 23 (10): 1641-1651.
 14. Matsumura Y, Aizawa H, Shiraki-Iida T, Nagai R, Kuro-o M, Nabeshima Y: Identification of the Human Klotho Gene and Its Two Transcripts Encoding Membrane and Secreted Klotho Protein. *Biochemical and Biophysical Research Communications* 1998, 242 (3): 626-630.
 15. Alexander RT, Woudenberg-Vrenken TE, Buurman J, Dijkman H, van der Eerden BC, van Leeuwen JP, Bindels RJ, Hoenderop JG: Klotho Prevents Renal Calcium Loss. *Journal of the American Society of Nephrology* 2009, 20 (11): 2371-2379.
 16. Nakatani T, Sarraj B, Ohnishi M, Densmore MJ, Taguchi T, Goetz R, Mohammadi M, Lanske B, Razzaque MS: *In vivo* genetic evidence for klotho-dependent, fibroblast growth factor 23 (Fgf23) -mediated regulation of systemic phosphate homeostasis. *FASEB Journal* 2009, 23 (2): 433-441.
 17. Yoshida T, Fujimori T, Nabeshima Y: Mediation of Unusually High Concentrations of 1,25-Dihydroxyvitamin D in Homozygous *klotho* Mutant Mice by Increased Expression of Renal 1 α -Hydroxylase Gene. *Endocrinology* 2002, 143 (2): 683-689.
 18. Strom M, Sandgren ME, Brown TA, DeLuca HF: 1,25-Dihydroxyvitamin D₃ up-regulates the 1,25-dihydroxyvitamin D₃ receptor *in vivo*. *Proceedings of the National Academy of Sciences of the United States of America* 1989, 86 (24): 9770-9773.
 19. Wiese RJ, Uhland-Smith A, Ross TK, Prah J, DeLuca HF: Up-regulation of the Vitamin D Receptor in Response to 1,25-Dihydroxyvitamin D₃ Results from Ligand-induced Stabilization. *The Journal of Biological Chemistry* 1992, 267 (28): 20082-20086.

20. Yao J, Kathpalia P, Bushinsky DA, Favus MJ: Hyperresponsiveness of vitamin D receptor gene expression to 1,25-dihydroxyvitamin D₃. A new characteristic of genetic hypercalciuric stone-forming rats. *The Journal of Clinical Investigation* 1998, 101 (10): 2223-2232.
21. Bustin M: Regulation of DNA-Dependent Activities by the Functional Motifs of the High-Mobility-Group Chromosomal Proteins. *Molecular and Cellular Biology* 1999, 19 (8): 5237-5246.
22. Bonaldi T, Langst G, Strohner R, Becker PB, Bianchi ME: The DNA chaperone HMGB1 facilitates ACF/CHRAC-dependent nucleosome sliding. *The EMBO Journal* 2002, 21 (24): 6865-6873.
23. Travers AA: Priming the nucleosome: a role for HMGB proteins? *EMBO Reports* 2003, 4 (2): 131-136.
24. Hock R, Furusawa T, Ueda T, Bustin M: HMG chromosomal proteins in development and disease. *Trends in Cell Biology* 2007, 17 (2): 72-79.
25. Tsung A, Sahai R, Tanaka H, Nakao A, Fink MP, Lotze MT, Yang H, Li J, Tracey KJ, Geller DA *et al*: The nuclear factor HMGB1 mediates hepatic injury after murine liver ischemia-reperfusion. *The Journal of Experimental Medicine* 2005, 201 (7): 1135-1143.
26. Li J, Gong Q, Zhong S, Wang L, Guo H, Xiang Y, Ichim TE, Wang CY, Chen S, Gong F *et al*: Neutralization of the extracellular HMGB₁ released by ischaemic damaged renal cells protects against renal ischaemia-reperfusion injury. *Nephrology Dialysis Transplantation* 2011, 26 (2): 469-478.
27. Low TL, Hu SK, Goldstein AL: Complete amino acid sequence of bovine thymosin β_4 : A thymic hormone that induces terminal deoxynucleotidyl transferase activity in thymocyte populations. *Proceedings of the National Academy of Sciences of the United States of America* 1981, 78 (2): 1162-1166.
28. Paulussen M, Landuyt B, Schoofs L, Luyten W, Arckens L: Thymosin beta 4 mRNA and peptide expression in phagocytic cells of different mouse tissues. *Peptides* 2009, 30 (10): 1822-1832.
29. Malinda KM, Goldstein AL, Kleinman HK: Thymosin β_4 stimulates directional migration of human umbilical vein endothelial cells. *FASEB Journal* 1997, 11 (6): 474-481.
30. Malinda KM, Sidhu GS, Mani H, Banaudha K, Maheshwari RK, Goldstein AL,

- Kleinman HK: Thymosin β_4 Accelerates Wound Healing. *Journal of Investigative Dermatology* 1999, 113 (3): 364-368.
31. Goldstein AL, Hannappel E, Kleinman HK: Thymosin β_4 : actin-sequestering protein moonlights to repair injured tissues. *Trends in Molecular Medicine* 2005, 11 (9): 421-429.
 32. Cha HJ, Jeong MJ, Kleinman HK: Role of Thymosin β_4 in Tumor Metastasis and Angiogenesis. *Journal of the National Cancer Institute* 2003, 95 (22): 1674-1680.
 33. Gemoll T, Strohkamp S, Schillo K, Thorns C, Habermann JK: MALDI-imaging reveals thymosin beta-4 as an independent prognostic marker for colorectal cancer. *Oncotarget* 2015.
 34. Gruner BM, Hahne H, Mazur PK, Trajkovic-Arsic M, Maier S, Esposito I, Kalideris E, Michalski CW, Kleeff J, Rauser S *et al*: MALDI Imaging Mass Spectrometry for *In Situ* Proteomic Analysis of Preneoplastic Lesions in Pancreatic Cancer. *PLoS One* 2012, 7 (6): e39424.
 35. Dunlop MH, Dray E, Zhao W, Tsai MS, Wiese C, Schild D, Sung P: RAD51-associated Protein 1 (RAD51AP1) Interacts with the Meiotic Recombinase DMC1 through a Conserved Motif. *The Journal of Biological Chemistry* 2011, 286 (43): 37328-37334.
 36. Dray E, Dunlop MH, Kauppi L, San Filippo J, Wiese C, Tsai MS, Begovic S, Schild D, Jasin M, Keeney S *et al*: Molecular basis for enhancement of the meiotic DMC1 recombinase by RAD51 associated protein 1 (RAD51AP1). *Proceedings of the National Academy of Sciences of the United States of America* 2011, 108 (9): 3560-3565.
 37. Wiese C, Dray E, Groesser T, San Filippo J, Shi I, Collins DW, Tsai MS, Williams GJ, Rydberg B, Sung P *et al*: Promotion of Homologous Recombination and Genomic Stability by RAD51AP1 via RAD51 Recombinase Enhancement. *Molecular cell* 2007, 28 (3): 482-490.
 38. Lombard DB, Chua KF, Mostoslavsky R, Franco S, Gostissa M, Alt FW: DNA Repair, Genome Stability, and Aging. *Cell* 2005, 120 (4): 497-512.
 39. Hudson D, Kovalchuk I, Koturbash I, Kolb B, Martin OA, Kovalchuk O: Induction and persistence of radiation-induced DNA damage is more pronounced in young animals than in old animals. *Aging* 2011, 3 (6): 609-620.

40. Yamamoto M, Clark JD, Pastor JV, Gurnani P, Nandi A, Kurosu H, Miyoshi M, Ogawa Y, Castrillon DH, Rosenblatt KP *et al*: Regulation of Oxidative Stress by the Anti-aging Hormone Klotho. *The Journal of Biological Chemistry* 2005, 280 (45): 38029-38034.
41. Lim JH, Kim EN, Kim MY, Chung S, Shin SJ, Kim HW, Yang CW, Kim YS, Chang YS, Park CW *et al*: Age-Associated Molecular Changes in the Kidney in Aged Mice. *Oxidative Medicine and Cellular Longevity* 2012, 2012: 171383.
42. Zuo Z, Lei H, Wang X, Wang Y, Sonntag W, Sun Z: Aging-related kidney damage is associated with a decrease in klotho expression and an increase in superoxide production. *Age* 2011, 33 (3): 261-274.
43. Cadigan KM, Nusse R: Wnt signaling: a common theme in animal development. *Genes & Development* 1997, 11 (24): 3286-3305.
44. He W, Dai C, Li Y, Zeng G, Monga SP, Liu Y: Wnt/ β -Catenin Signaling Promotes Renal Interstitial Fibrosis. *Journal of the American Society of Nephrology* 2009, 20 (4): 765-776.
45. Liu H, Fergusson MM, Castilho RM, Liu J, Cao L, Chen J, Malide D, Rovira, II, Schimel D, Kuo CJ *et al*: Augmented Wnt Signaling in a Mammalian Model of Accelerated Aging. *Science* 2007, 317 (5839): 803-806.
46. Kusakabe T, Motoki K, Hori K: Mode of Interactions of Human Aldolase Isozymes with Cytoskeletons. *Archives of Biochemistry and Biophysics* 1997, 344 (1): 184-193.
47. St-Jean M, Izard T, Sygusch J: A Hydrophobic Pocket in the Active Site of Glycolytic Aldolase Mediates Interactions with Wiskott-Aldrich Syndrome Protein. *The Journal of Biological Chemistry* 2007, 282 (19): 14309-14315.
48. Tochio T, Tanaka H, Nakata S, Hosoya H: Fructose-1,6-bisphosphate aldolase A is involved in HaCaT cell migration by inducing lamellipodia formation. *Journal of Dermatological Science* 2010, 58 (2): 123-129.
49. Caspi M, Perry G, Skalka N, Meisel S, Firsow A, Amit M, Rosin-Arbesfeld R: Aldolase positively regulates of the canonical Wnt signaling pathway. *Molecular Cancer* 2014, 13: 164.
50. Ozawa H, Takata K: The Granin Family – Its Role in Sorting and Secretory Granule Formation. *Cell Structure and Function* 1995, 20 (6): 415-420.
51. Lloyd RV, Cano M, Rosa P, Hille A, Huttner WB: Distribution of chromogranin

- A and secretogranin I (chromogranin B) in neuroendocrine cells and tumors. *The American Journal of Pathology* 1988, 130 (2): 296-304.
52. Nobels FR, Kwekkeboom DJ, Bouillon R, Lamberts SW: Chromogranin A: its clinical value as marker of neuroendocrine tumours. *European Journal of Clinical Investigation* 1998, 28 (6): 431-440.
 53. Ramachandran R, Bech P, Murphy KG, Caplin ME, Patel M, Vohra S, Khan MS, Dhillon WS, Sharma R, Palazzo FF *et al*: Comparison of the Utility of Cocaine- and Amphetamine-Regulated Transcript (CART), Chromogranin A, and Chromogranin B in Neuroendocrine Tumor Diagnosis and Assessment of Disease Progression. *The Journal of Clinical Endocrinology and Metabolism* 2015, 100 (4): 1520-1528.
 54. Capellino S, Lowin T, Angele P, Falk W, Grifka J, Straub RH: Increased chromogranin A levels indicate sympathetic hyperactivity in patients with rheumatoid arthritis and systemic lupus erythematosus. *The Journal of Rheumatology* 2008, 35 (1): 91-99.
 55. Oberg K: Neuroendocrine gastrointestinal tumours. *Annals of Oncology* 1996, 7 (5): 453-463.
 56. Kang SW: Adrenergic Genetic Mechanisms in Hypertension and Hypertensive Kidney Disease. *Electrolyte & Blood Pressure* 2013, 11 (1): 24-28.
 57. Crippa L, Bianco M, Colombo B, Gasparri AM, Ferrero E, Loh YP, Curnis F, Corti A: A new chromogranin A-dependent angiogenic switch activated by thrombin. *Blood* 2013, 121 (2): 392-402.
 58. Ballermann BJ, Obeidat M: Tipping the balance from angiogenesis to fibrosis in CKD. *Kidney International Supplements* 2014, 4 (1): 45-52.
 59. Velez JC, Janech MG, Hicks MP, Morinelli TA, Rodgers J, Self SE, Arthur JM, Fitzgibbon WR: Lack of Renoprotective Effect of Chronic Intravenous Angiotensin-(1-7) or Angiotensin-(2-10) in a Rat Model of Focal Segmental Glomerulosclerosis. *PLoS One* 2014, 9 (10): e110083.
 60. Fukuda A, Wickman LT, Venkatarreddy MP, Sato Y, Chowdhury MA, Wang SQ, Shedden KA, Dysko RC, Wiggins JE, Wiggins RC: Angiotensin II-dependent persistent podocyte loss from destabilized glomeruli causes progression of end stage kidney disease. *Kidney International* 2012, 81 (1): 40-55.
 61. Rosjto H, Husberg C, Dahl MB, Stridsberg M, Sjaastad I, Finsen AV, Carlson

CR, Oie E, Omland T, Christensen G: Chromogranin B in Heart Failure: A Putative Cardiac Biomarker Expressed in the Failing Myocardium. *Circulation: Heart Failure* 2010, 3 (4): 503-511.

62. Labeit S, Kolmerer B: Titins: Giant Proteins in Charge of Muscle Ultrastructure and Elasticity. *Science* 1995, 270 (5234): 293-296.

Chapter 2

Imaging and mapping of Klotho-deficient mouse bone using MALDI imaging mass spectrometry

1. Abstract

Matrix-assisted laser desorption/ionization-imaging mass spectrometry (MALDI-IMS) is an advanced method used globally for analyzing the distribution of biomolecules on tissue cryosections without any probes. Hydroxyapatite crystals in bones make it difficult to determine the distribution of biomolecules using MALDI-IMS, and there is limited information regarding the use of this method to analyze bones. To determine if MALDI-IMS analysis of bone tissues can aid in comprehensive mapping of biomolecules in mouse bone, and identify anomalous metabolites in the bone of Klotho-deficient ($kl^{-/-}$) mice with osteopenia, first, the femurs and/or tibiae from 8-week-old male mice were fixed and decalcified in various combinations of fixation and decalcification solutions. Fresh samples with or without decalcification were also prepared. About 10- μ m thick cryosections were mounted on ITO-coated glass slides, dried, and matrix solution was sprayed on the tissue surface. The images were acquired using iMScope (Shimadzu) within a mass-to-charge range of 100 to 1000. Adjacent sections were stained with Hematoxylin-Eosin, Alcian blue, Azan, and PAS to evaluate the histological and histochemical features. Femurs from $kl^{-/-}$ mice were fixed/decalcified in trichloroacetic acid (TCA) and used for MALDI-IMS and MS-MS analyses. The results were compared with those obtained for wild-type mice. Among various fixation and decalcification conditions, sections from TCA-treated samples

were most suitable to examine both the histology and comprehensive MS images. However, histotypic MS signals were detected in all sections. The MS-MS analysis revealed product ions that are unique to Klotho-deficient mice. In addition to the MS images, 2-hydroxyestradiol was identified as a candidate metabolite that is involved in skeletal defects of *kl^{-/-}* mice. These results indicate successful detection of biomolecules in bone using MALDI-IMS. Although analytical procedures and compositional adjustment regarding the performance of the device still requires further development, IMS appears to be a powerful tool to determine the distribution of biomolecules even in the bone tissues.

2. Introduction

Hard tissues such as bones and teeth are calcified tissues. Therefore, it is difficult using cellular and molecular analyses to investigate the function of cells such as osteocytes and cementocytes, and the distribution of organic matter such as proteins and peptides. For example, osteocytes, which terminally differentiate from osteoblasts and are embedded into the bone matrix play an important role in the maintenance of homeostasis in the network between osteoblasts and osteoclasts [1]. To confirm the physiological function of osteocytes, it is preferable to retain the original distribution of biomolecules when analyzed. In that context, matrix-assisted laser desorption/ionization imaging mass spectrometry (MALDI-IMS) is a useful method for investigation; MALDI-IMS enables analyzing the distribution of molecules without any disruption in the morphology and architecture. The benefit of MALDI-IMS for discovering the novel pathological molecules has already been described in **Chapter 1**. MALDI-IMS, however, has certain limitations for quantitative and qualitative uncertainty analysis. Additionally, there are few studies that used MALDI-IMS for bone tissues to identify the molecules because of the lack of appropriate methods to prepare sections for ionization [2-4]. Hirano et al. reported MALDI-IMS for tooth cryosections sliced by the Kawamoto method using adhesive film without any pretreatment such as fixation and decalcification [2]; however, the signals obtained from the enamel and dentin were not listed in the metabolomics database. They concluded that almost all of these signals are mineral, which can interrupt the ionization of the large components. Therefore, this study attempts to establish an appropriate protocol for the fixation and/or decalcification of samples derived from bone to detect MS using MALDI-IMS and provide a comprehensive mapping of proteins and peptides.

Klotho gene mutation leads to a syndrome that is similar to accelerated human aging,

including ectopic calcification and osteoporosis [5] (see **Chapter 1**). Klotho acts as a cofactor for fibroblast growth factor (FGF) 23, which is mainly derived from the osteolineage cells [6] to increase the affinity of FGF23 to the FGF receptors [7]. The principle function of FGF23 is to maintain homeostasis in phosphate and vitamin D metabolism by regulating the sodium phosphate co-transporter and vitamin D-metabolizing enzymes in the kidneys [8], however, recent studies indicated that FGF23 directly regulates bone mineralization in both Klotho-dependent and independent manners [9, 10]. It was also reported that soluble Klotho, cleaved by A Disintegrin, as well as Metalloproteinase (ADAM) 10 and ADAM17 [11] acts to protect from uremic cardiomyopathy, inhibit renal inflammation, and suppress tumor growth independent of FGF23 [12-14]. In this study, we also attempt to identify anomalous metabolites in bone of Klotho-deficient ($kl^{-/-}$) mice with osteopenia.

3. Materials and Methods

3.1. Materials

Conductive ITO (indium tin oxide)-coated glass slides (8-12 Ω) were purchased from Sigma–Aldrich Co. (St. Louis, MO). α -Cyano-4-hydroxycinnamic acid (CHCA) matrices were purchased from Bruker Daltonics (Bremen, Germany). Carboxymethylcellulose (CMC, 2 %) was purchased from Leica Microsystems (Wetzlar, Germany). Trifluoroacetic acid (TFA), 2,5-Dihydroxy-benzoic acid (DHB) and all other chemicals, unless otherwise specified, were purchased from Sigma–Aldrich Co..

3.2. Animals

Klotho heterozygous ($kl^{+/+}$) and C57BL/6J mice were purchased from CLEA Inc. (Osaka, Japan). $kl^{-/-}$ mice were obtained by mating the $kl^{+/+}$ mice. Mice were housed and handled to minimize pain or discomfort to animals according to protocols approved by Institutional Animal Care and Use Committee at the Central Institute for Experimental Animals and the Committee of Animal Experimentation at Hiroshima University. Genotyping of *Klotho* knockout mice and *Klotho* wild-type was done as described [15].

3.3. Specimen preparation

Femurs and/or tibiae from 8-week-old male mice (C57BL/6) were fixed and decalcified in various combinations of fixation and decalcification solutions (e.g., 4% paraformaldehyde (PFA), Carnoy fluid, trichloroacetic acid (TCA) for fixation; formic acid, EDTA-NH₄, and TCA for decalcification) (see **Table 1**). Fresh samples with or without decalcification were also prepared. Samples were then embedded in a stainless steel container filled with 2% CMC and placed in dry ice-cooled hexane to make frozen CMC blocks. Each frozen block was stored at -80°C until sectioning. Tissues were sectioned (5 μm for staining and MALDI-IMS of fresh samples without any

pretreatment by Kawamoto method [16], and 10 μm for MALDI-IMS of samples with pretreatment) with a CM 3050 S cryostat (Leica Microsystems). For staining, sections were placed on the normal glass slides and washed with 100 % ethanol. For MALDI-IMS, sections were placed on Indium-tin-oxide (ITO)-coated glass slides (with electrically conducting double-adhesive tape for samples without pretreatment), followed by washing with 70 % ethanol and 100 % ethanol, and drying. Femurs from *kl^{-/-}* mice were fixed/decalcified in TCA, followed by the same method as described above.

3.4. Staining

Adjacent sections were stained with Hematoxylin-Eosin (H-E), Alcian blue, Azan, and PAS to evaluate histological and histochemical features. Sections without fixation were fixed with 4% PFA.

3.5. MALDI-IMS and MS-MS

After cryosections were dried at room temperature, sections were coated with DHB or CHCA matrix vapor deposition using iMlayer (Shimadzu Corporation, Kyoto, Japan) at a thickness of 1.5 or 0.7 μm , respectively. MALDI images were acquired using iMScope (Shimadzu) in positive or negative ion mode in a range of m/z (mass-to-charge ratio) of 100 to 1000 at 1000 Hz laser frequency accumulating 50 laser shots. The detector voltage and sample voltage were 1.7 to 1.9 kV and 3.0 to 3.5 kV, respectively. Spatial resolution was 10 μm and laser intensity was 23 to 45. To omit the influence of fixing and decalcifying solutions and matrices, 1 μL of mixture of each solution and matrix was placed onto a stainless-steel (SUS) plate and supplied to iMScope after drying. Mass spectra obtained from this mixture were omitted from those from the samples. MS-MS data were evaluated using the Human Metabolome Database (HMDB) search engine (version 3.6, The Metabolomics Innovation Centre, AB, Canada) for metabolite identification.

4. Results

4.1. Histological and histochemical features of bones with or without pretreatment

To evaluate the influence of fixing and/or decalcifying solutions on histological and histochemical features of femurs and tibiae, the cryosections were stained with H-E, Alcian blue, Azan, and PAS. Compared to the section without any pretreatment with H-E staining, (**Figure 1A**), cell swelling was seen and the shape of cells was unclear. Among various fixation and decalcification conditions, sections from TCA-treated samples were most suitable for examining both histology and comprehensive MS images (**Figure 1B**), followed by the samples decalcified with EDTA after fixation than others (**Figures 1C, D**). Bone marrows were peeled from trabecular bone surfaces in the samples with formic acid decalcification (**Figures 1E, F**). Cartilages in the growth plate and bone marrows were unable to keep their structure in samples with decalcification without fixation (**Figures 1G, H**). There was no difference between all samples with Azan and PAS staining. With Alcian Blue staining, however, bone marrows in unfixed and Carnoy/EDTA-treated samples turned dark blue (**Figure 1 A, D, G, and H**).

4.2. Comparison of MALDI-IMS between bones with or without pretreatment

To set up the measurement conditions of MALDI-IMS, all samples were supplied to iMScope in positive or negative ion mode with DHB or CHCA matrix. Among these, the condition of positive mode with DHB was enabled to detect many mass spectra in the wide range of m/z (**Figure 2 A-D**, in the case of sample with TCA treatment). Imaging by MALDI-IMS showed tissue-specific distribution of MS with DHB (**Figure 2E**). Because the Kawamoto method requires cryofilm, MALDI-IMS of TCA-treated sections mounted on ITO-coated glass slide with or without cryofilm were analyzed to check the interference of cryofilm. With cryofilm, the number of mass spectra was much less than without cryofilm (**Figure 2F, G**).

In comparison of mass spectra detected in positive ion mode with DHB, the undecalcified sample with the Kawamoto method exhibited few peaks in the range of m/z 100-700 (**Figure 3A**). Each section has its own characteristic features of the appearance of peaks, but there was no significant difference in the obtained number of mass spectra between decalcified and/or fixed samples (**Figures 3B-H**).

In MALDI-IMS, histotypic MS signals were detected in all sections. The signals of the molecule at m/z 554.57 was located mainly in bone marrows in all sections except the undecalcified section, and the molecule at m/z 185.13 was located mainly in cortical bones, trabecular bones, and cartilages in all sections except the Carnoy/formic acid sample (**Figure 4**). In the undecalcified section, there was a few signals at m/z 554.57 (**Figure 4A**), and the signals at m/z 185.13 were localized diffusely in the Carnoy/formic acid sample (**Figure 4F**).

By using Principal Component Analysis (PCA), a statistical method to extract the first principal component in variance between the samples, the first principal component was the same in the samples except the undecalcified, Carnoy/EDTA, and PFA/formic acid samples in the range of m/z 100-700 (**Table 2**).

4.3. Metabolomics with WT and $kl^{-/-}$ mouse femurs

To identify the anomalous metabolites in the bones of $kl^{-/-}$ mice, the TCA-treated sections from wild-type (WT) and $kl^{-/-}$ mouse femurs were applied to iMScope in positive ion mode with the DHB matrix. Several different mass spectra were obtained between genotypes in bones (**Figure 5A, B**), cartilages (**Figure 5C, D**), and bone marrows (**Figure 5E, F**). Because m/z 289.1 and m/z 300.1 were specifically located in the bones and cartilages of $kl^{-/-}$ mice femurs in MALDI-IMS (**Figure 6**), these two molecules were selected as precursor ions for MS-MS analysis to search the product

ions by using HMDB. As a result, m/z 289.1 and m/z 300.1 were identified as 2-hydroxyestradiol and sphingosine, respectively (**Table 3**), suggesting that these metabolites may be involved in skeletal defects in $kl^{-/-}$ mice.

5. Discussion

This study comprehensively determined the metabolomics of the *kl^{-/-}* mouse bone to identify novel pathologic factors with localization information using MALDI-IMS with fixation and decalcification.

When preparing the cryosections of hard tissues without decalcification, the Kawamoto method requires cryofilm which can attach to the cutting surface under the freezing conditions [16]. Furthermore, for ionization, an electrically conducting double-adhesive tape is needed to set sections on the ITO-glass slide [2]. In a comparison of mass spectra between the sections with or without the tape, many more peaks were obtained from the section without the tape than another one. A method to remove the tape before applying to MALDI-IMS is reported [4], but a high degree of technical skill is required to do so.

For MALDI-IMS, the fresh (without fixation) frozen sections were usually used for analysis. This study shows that the fixation and decalcification of bones makes preparation of sections easier and detection of MS from organic components is possible because of removing minerals. Since the usefulness of MALDI-IMS of formaline-fixed paraffin-embedded (FFPE) tissues was reported [17], the researchers have focused on analysis with FFPE samples in MALDI-IMS [18-24]. Formalin fixation can be used to avoid degradation and spoilage of samples, however, the cross-linked molecules between formalin and primary amines are unable to be ionized. Therefore, the number of identified proteins from FFPE sections is less than in cryosections, and several steps for removing formalin, breaking cross links, and cleaving of proteins to peptides are required [18, 24, 25]. If the targets are nucleotides, lipids, and peptides without primary amines, formalin does not form the cross-link and it is possible to apply the samples without such steps. Organic solvents such as ethanol can also fix the tissues by

coagulation and precipitation of proteins. Fixation with organic solvents has less interruption for MALDI-IMS, but dissolves away lipids from tissues. Based on these, fixation solution must be selected according to an object to be analyzed.

Decalcification with EDTA or TCA was better than with formic acid to keep the tissue structures. Bone marrows were peeled from trabecular bone surfaces by formic acid decalcification, which can occur during the preparation of sections [26]. Treatment with TCA is useful because of a rapid one-step fixation and decalcification, which can preserve antigen and tissue morphology [27]. In this study, sections from TCA-treated samples were most suitable for examining both histology and comprehensive MS images.

On the metabolomics of TCA-treated samples from *kl^{-/-}* mouse bone with MALDI-IMS, some biomolecules were identified. Among of these, 2-hydroxyestradiol and sphingosine were focused on. 2-hydroxyestradiol is one of metabolites of estrogen and an immediate precursor of 2-methoxyestradiol, and previous studies reported that 2-hydroxyestradiol inhibits osteoclast formation [28, 29]. Since both the number and the activity of osteoclasts are decreased in *kl^{-/-}* mouse bone [30], these studies support our results that 2-hydroxyestradiol is detectable in the *kl^{-/-}* mouse bone. The functions of sphingosine, a primary part of the sphingolipids, and its derivatives, including sphingosine 1 phosphate (S1P), on bone metabolism are complicated. In mouse calvaria-derived preosteoblast (MC3T3-E1) cultures, previous studies reported that sphingosine and S1P lead to intracellular calcium release [31, 32]. On the other hand, Kato et al. demonstrated that S1P induces heat shock protein 27, which has not only a stimulatory effect on mineralization but also an inhibitory effect on osteocalcin expression [33]. It is also suggested that S1P stimulates chondrocyte proliferation via ERK signaling in rat articular chondrocytes [34] and controls the migration of osteoclast precursors between bone tissues and the blood stream [35]. Further examination to

clarify the role of sphingosine in kT^{-} is needed.

This study successfully detected biomolecules in bones using MALDI-IMS. Although analytical procedures and compositional adjustment on device performance still require further development, MALDI-IMS appears to be a powerful tool for searching biomolecules even in bones.

6. Figure Legends

Figure 1. Histological observations of femur and tibia fixed and decalcified with each solution by H-E, Alcian blue, Azan, and PAS staining. (A), the sections of unfixed/undecalcified tibiae. (B), the sections of TCA-treated femurs. (C)-(H), the sections of femurs with treatment of PFA/EDTA (C), Carnoy/EDTA (D), PFA/formic acid (E), or Carnoy/formic (F). (G, H), the unfixed sections of femurs with formic acid (G) or EDTA (H) decalcification.

Figure 2. Mass spectra (maximum intensity) and MALDI-IMS of TCA-treated samples analyzed with MALDI-IMS in the range of m/z 100-1000 under the various conditions. (A, B), analysis with DHB matrix in the positive (A) or the negative (B) ion mode. (C, D), analysis with CHCA matrix in the positive (C) or the negative (D) ion mode. (E), imaging of histotypic distribution of several mass peaks on the sections. Left two images are of optical and H-E staining. (F, G), the mass spectra detected from the sections with (G) or without (F) a tape.

Figure 3. Mass spectra (maximum intensity) of each treatment with MALDI-IMS in the range of 100 to 1000 and the positive ion mode with DHB. (A), the sections of unfixed/undecalcified tibiae. (B), the sections of TCA-treated femurs. (C)-(H), the sections of femurs with treatment of PFA/EDTA (C), Carnoy/EDTA (D), PFA/formic acid (E), or Carnoy/formic (F). (G, H), the unfixed sections of femurs with formic acid (G) or EDTA (H) decalcification.

Figure 4. MALDI-IMS at m/z 554.57 and m/z 185.13 of each treatment. The left row indicates the optical images. (A), the sections of unfixed/undecalcified tibiae. (B), the sections of TCA-treated femurs. (C)-(H), the sections of femurs with treatment of

PFA/EDTA (C), Carnoy/EDTA (D), PFA/formic acid (E), or Carnoy/formic (F). (G, H), the unfixed sections of femurs with formic acid (G) or EDTA (H) decalcification.

Figure 5. Mass spectra (maximum intensity) detected by MALDI-IMS in range of 100 to 700 and the positive ion mode with DHA of TCA-treated femurs derived from WT and $kl^{-/-}$ mice. Region of interest was selected in bones (A, B), cartilages (C, D), and bone marrows (E, F) from WT (A, C, E) and $kl^{-/-}$ (B, D, F) mouse bone.

Figure 6. MALDI-IMS of femurs derived from $kl^{-/-}$ mouse at m/z 289.03 and m/z 300.08. Upper panels show optical image (A) and H-E staining (B). Lower panels show MALDI-IMS images at m/z 289.03 (C) and m/z 300.08 (D).

Figure 1

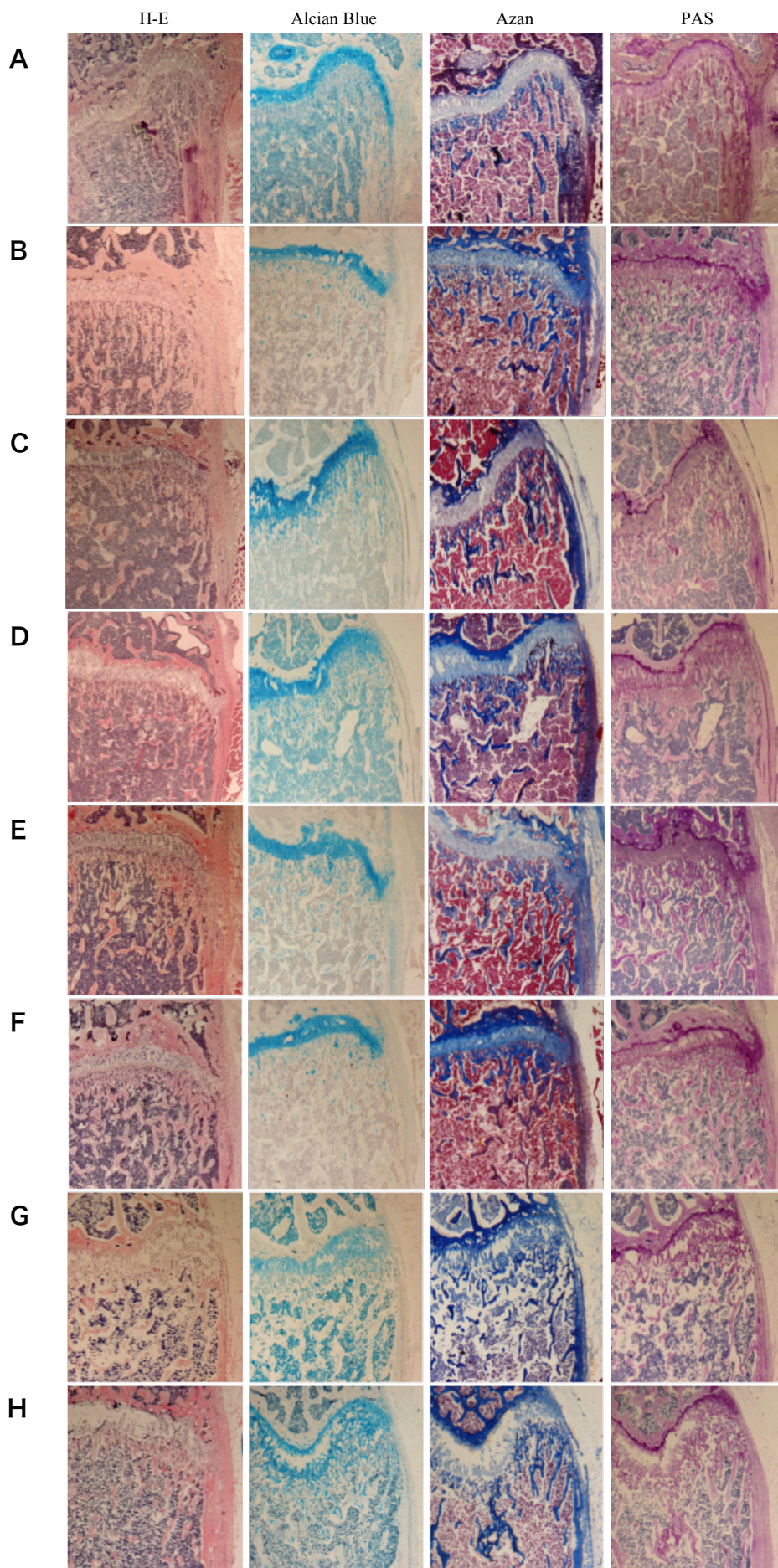


Figure 2

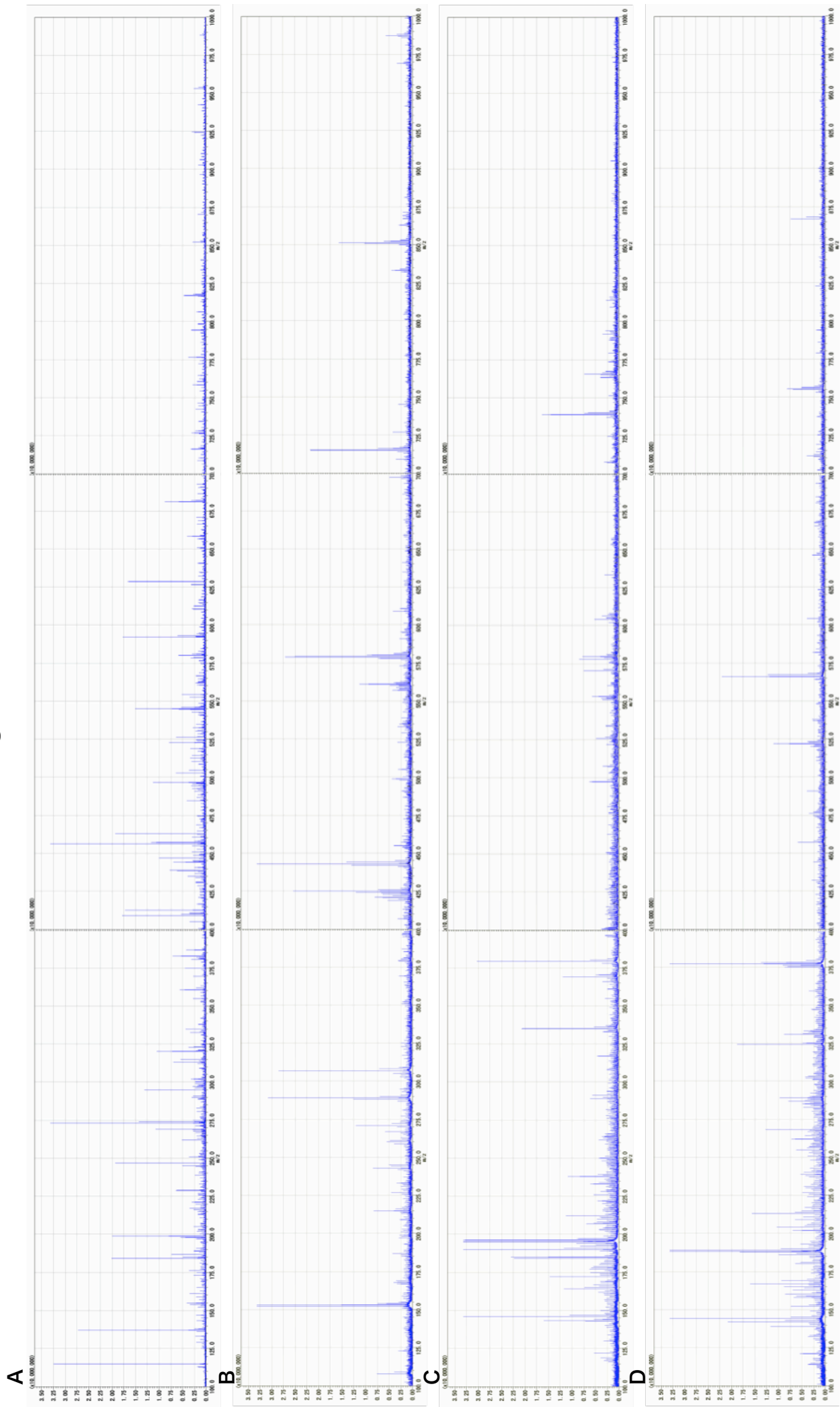
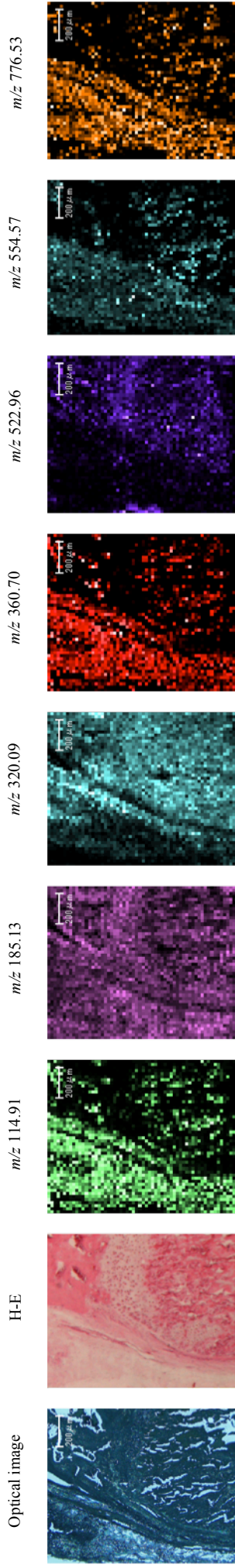
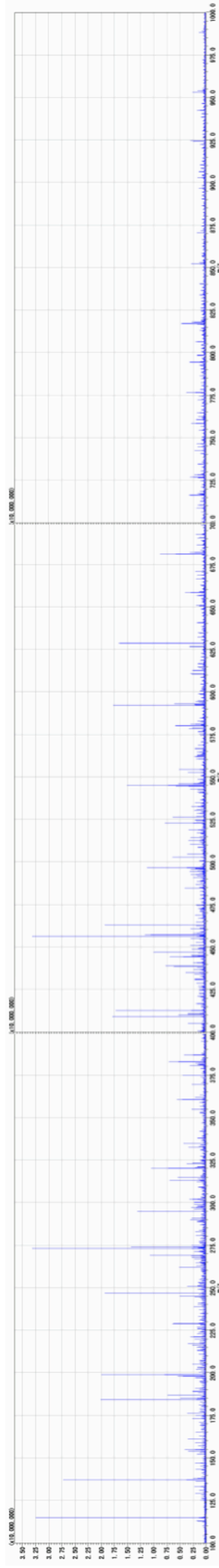


Figure 2 (Continued)

E



F



G



Figure 3

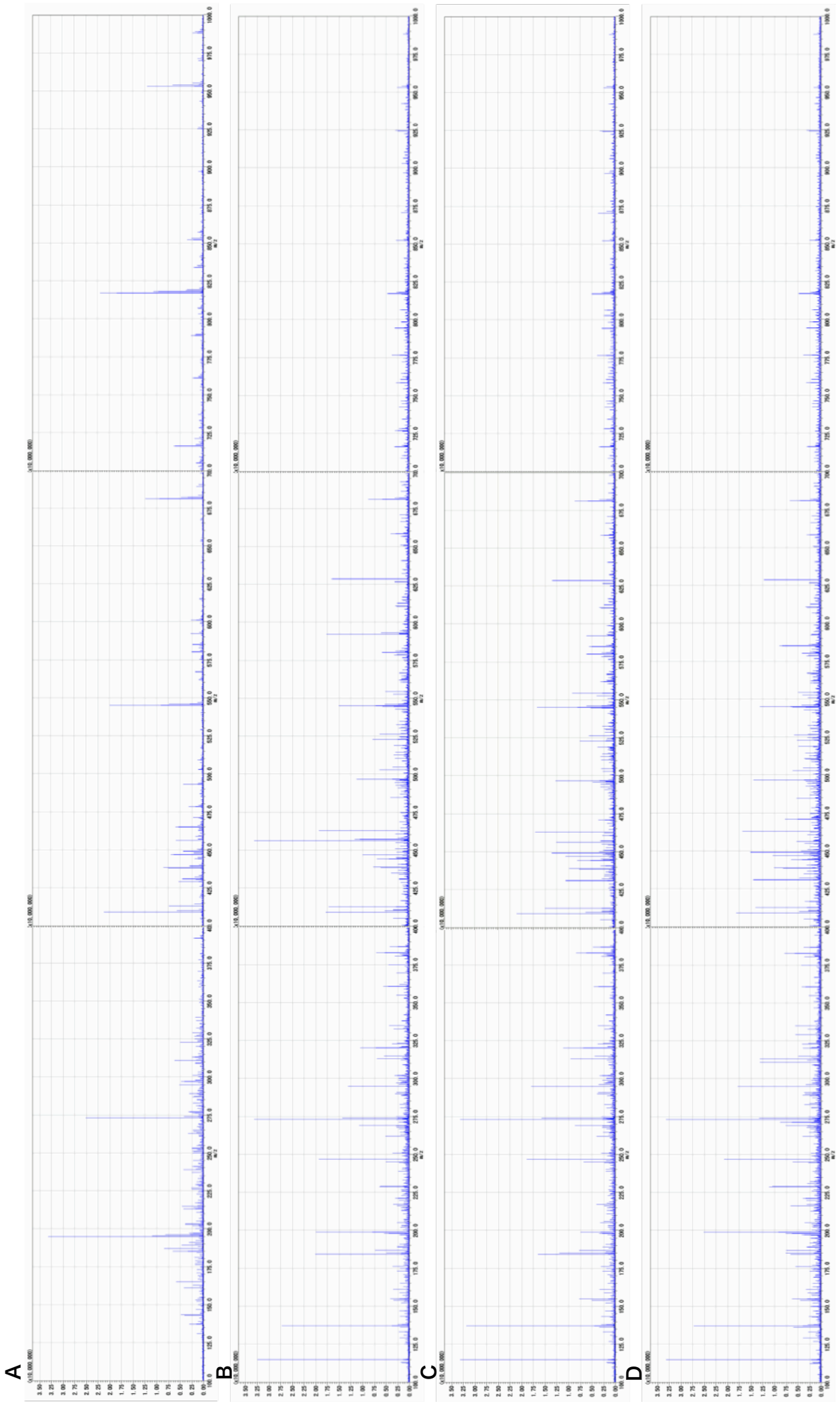


Figure 3 (Continued)

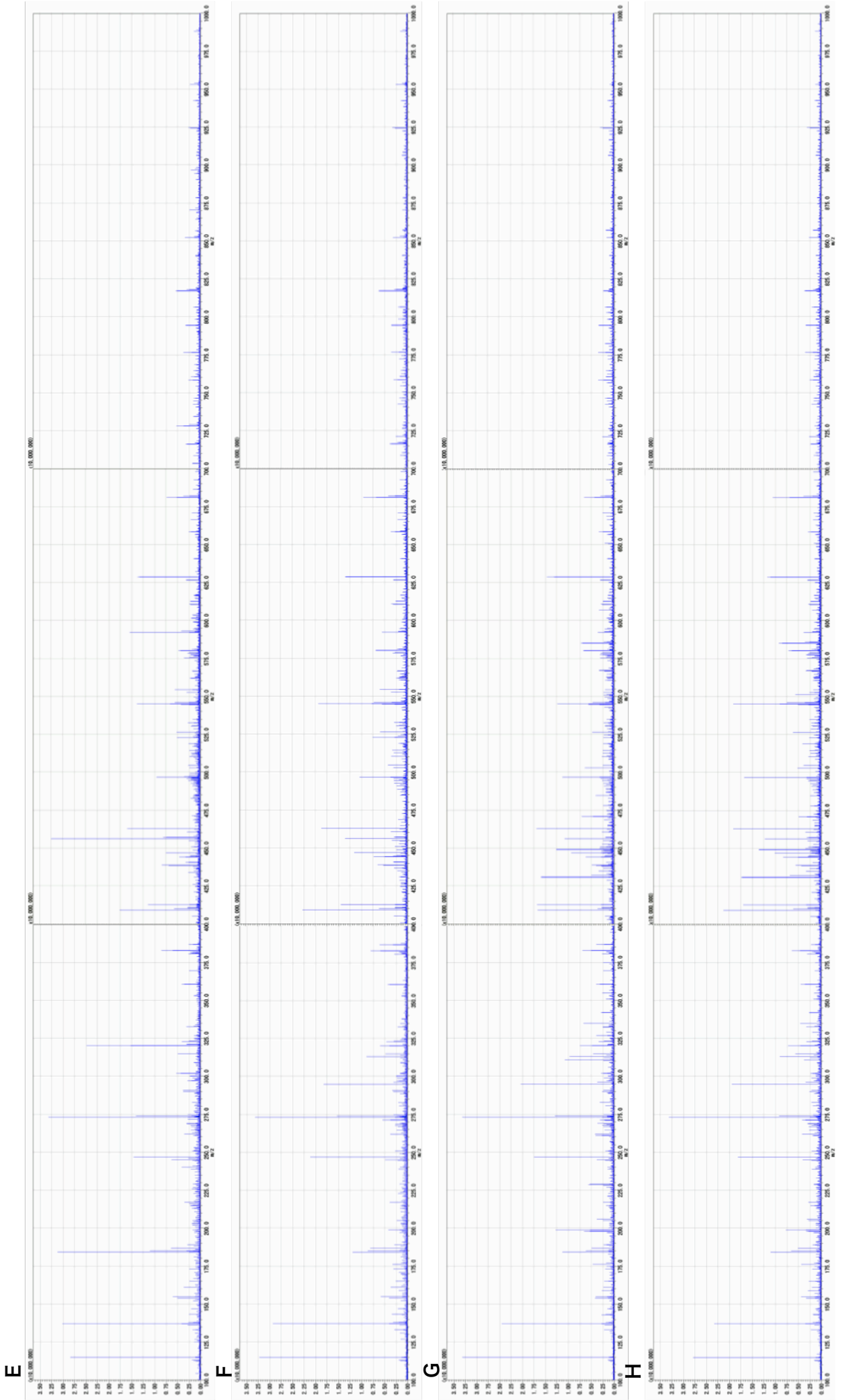


Figure 4

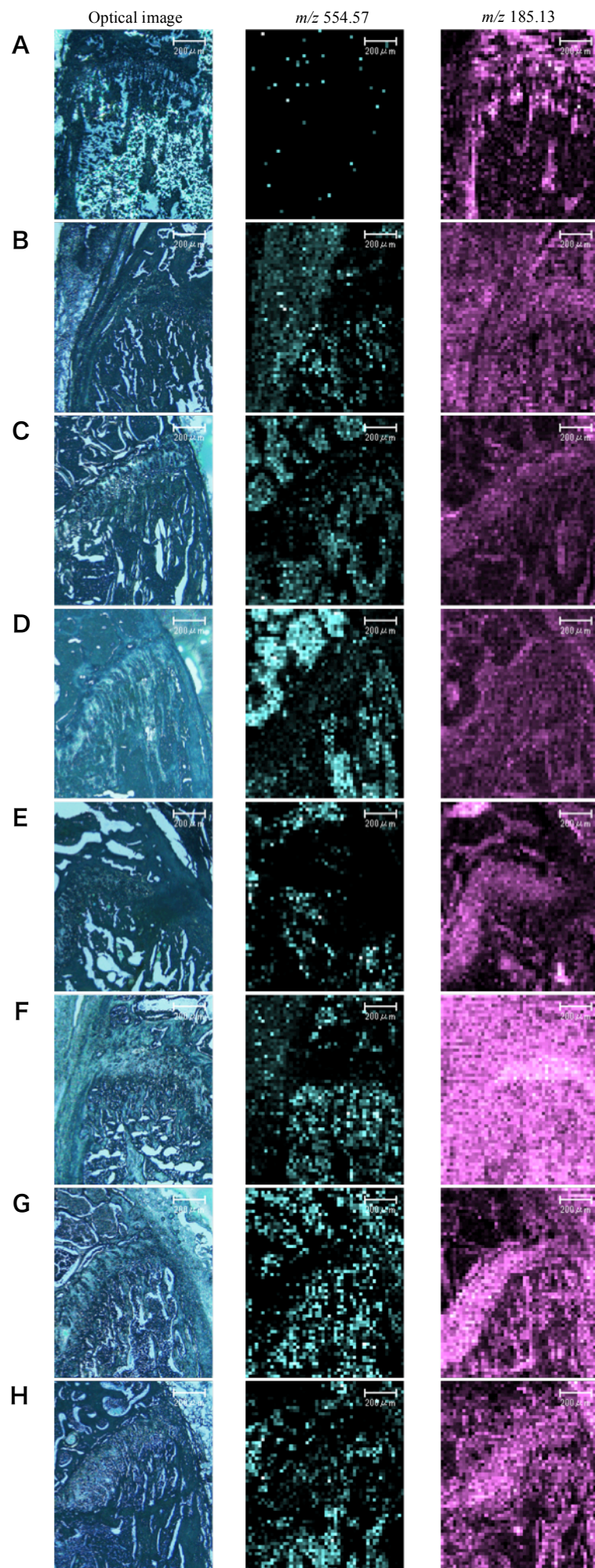


Figure 5

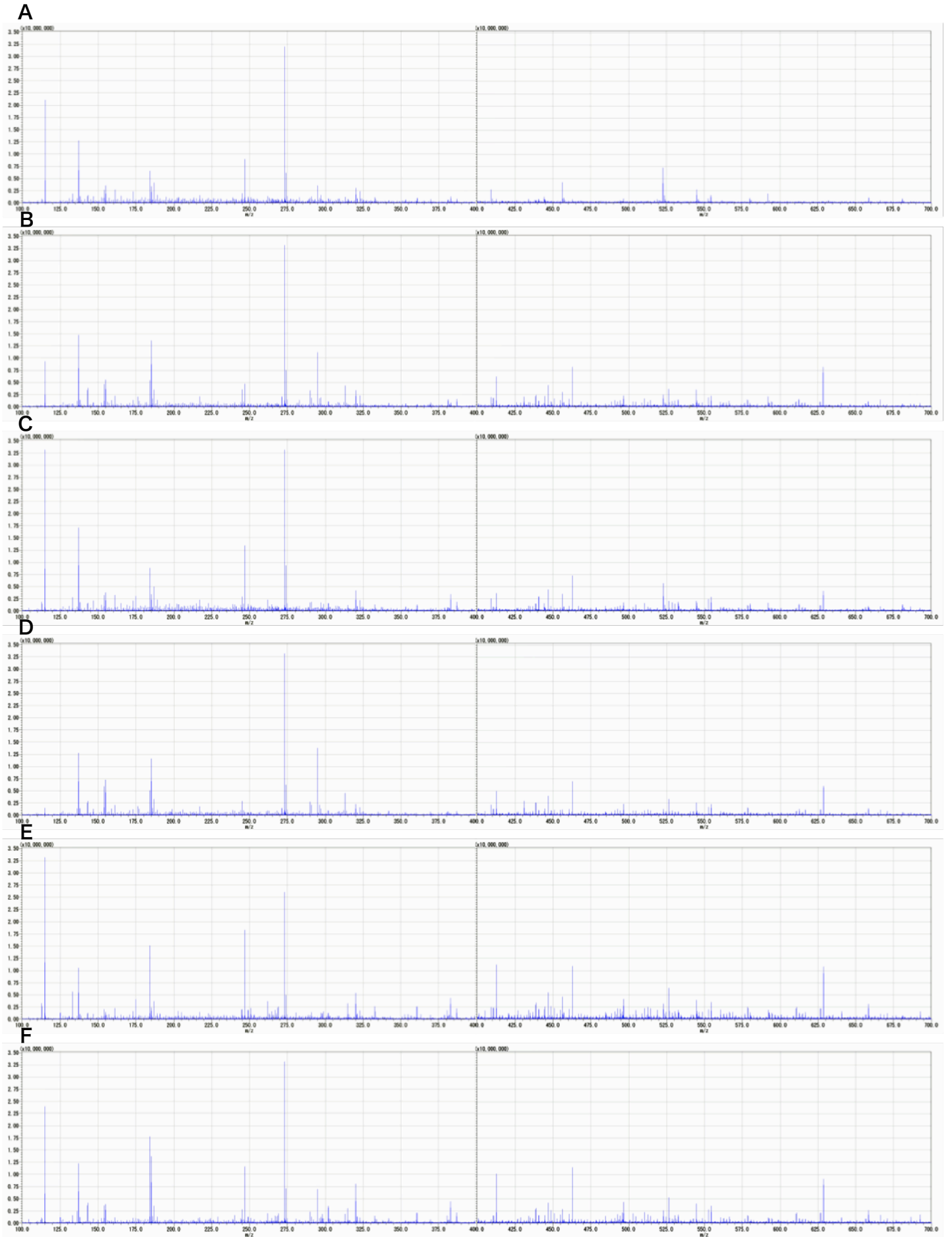


Figure 6

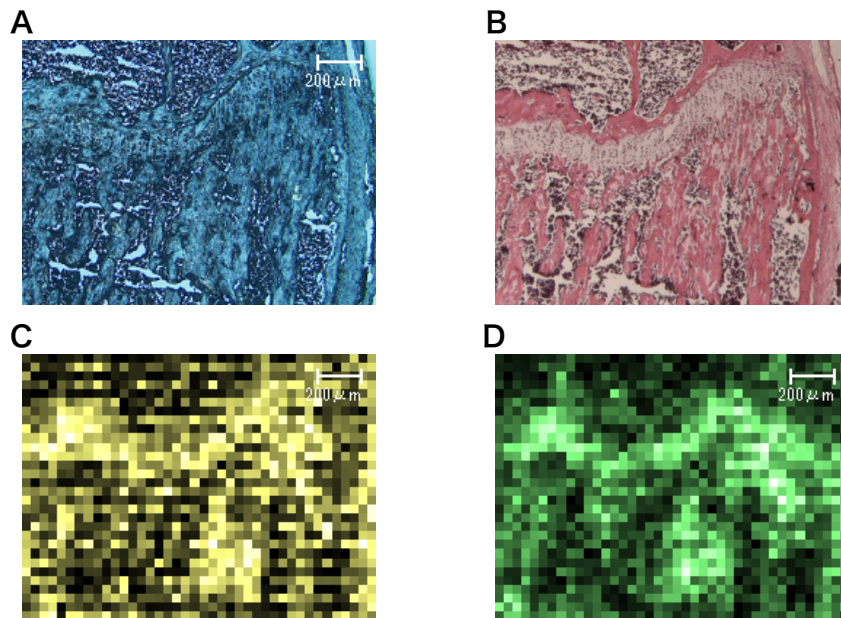


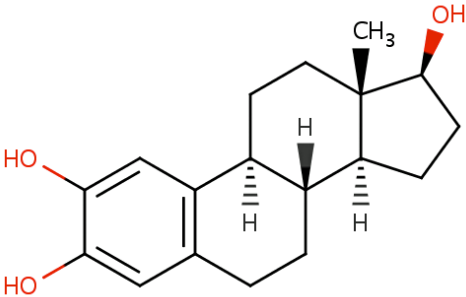
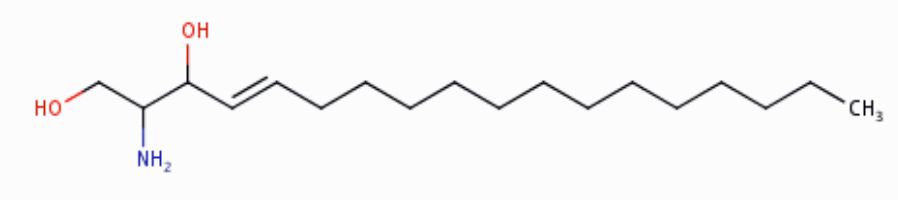
Table 1. Combinations of fixation and decalcification solutions

	A	B	C	D	E	F	G	H
Fixation	—	TCA, overnight	PFA, overnight	Carnoy, overnight	PFA, overnight	Carnoy, overnight	—	—
Decalcification	—		EDTA, 7 days	EDTA, 7 days	Formic acid, 2 days	Formic acid, 2 days	Formic acid, 2 days	EDTA, 4 days

Table 2. First principal component with or without pretreatment

	Unfixed/undecalcified	TCA	PFA/ EDTA	Carnoy/ EDTA	PFA/ Formic acid	Carnoy/ Formic acid	Unfixed/ Formic acid	Unfixed/ EDTA
<i>m/z</i> 100-400	165.07	114.91	114.91	114.91	184.08	114.91	114.91	114.91
<i>m/z</i> 400-700	456.11	462.73	462.73	412.71	462.73	462.73	462.73	462.73

Table 3. Metabolites estimated by HMDB

Name	Formula Weight	Structure
2-Hydroxyestradiol	288.3814 $C_{18}H_{24}O_3$	 <p>The structure of 2-Hydroxyestradiol is a steroid with a phenolic A ring. It features two hydroxyl groups (HO) at positions 2 and 3 on the A ring. The B ring has a double bond between C5 and C6. The D ring has a methyl group (CH₃) at C13 and a hydroxyl group (OH) at C14. Stereochemistry is indicated with wedges and dashes: H at C10 is dashed, H at C13 is dashed, and H at C14 is dashed.</p>
Sphingosine	299.4919 $C_{18}H_{37}NO_2$	 <p>The structure of Sphingosine is a long-chain amino alcohol. It consists of a sphingosine backbone with a primary hydroxyl group (HO) at C1, a secondary hydroxyl group (OH) at C2, and a primary amine group (NH₂) at C3. The chain continues with a double bond between C4 and C5, followed by a long saturated hydrocarbon chain ending in a methyl group (CH₃) at C24.</p>

8. References

1. Bonewald LF: The Amazing Osteocyte. *Journal of Bone and Mineral Research* 2011, 26 (2): 229-238.
2. Hirano H, Masaki N, Hayasaka T, Watanabe Y, Masumoto K, Nagata T, Katou F, Setou M: Matrix-assisted laser desorption/ionization imaging mass spectrometry revealed traces of dental problem associated with dental structure. *Analytical and Bioanalytical Chemistry* 2014, 406 (5): 1355-1363.
3. Cillero-Pastor B, Eijkel GB, Blanco FJ, Heeren RM: Protein classification and distribution in osteoarthritic human synovial tissue by matrix-assisted laser desorption ionization mass spectrometry imaging. *Analytical and Bioanalytical Chemistry* 2015, 407 (8): 2213-2222.
4. Seeley EH, Wilson KJ, Yankeelov TE, Johnson RW, Gore JC, Caprioli RM, Matrisian LM, Sterling JA: Co-registration of multi-modality imaging allows for comprehensive analysis of tumor-induced bone disease. *Bone* 2014, 61: 208-216.
5. Kuro-o M, Matsumura Y, Aizawa H, Kawaguchi H, Suga T, Utsugi T, Ohyama Y, Kurabayashi M, Kaname T, Kume E *et al*: Mutation of the mouse *klotho* gene leads to a syndrome resembling ageing. *Nature* 1997, 390 (6655): 45-51.
6. Yoshiko Y, Wang H, Minamizaki T, Ijuin C, Yamamoto R, Suemune S, Kozai K, Tanne K, Aubin JE, Maeda N: Mineralized tissue cells are a principal source of FGF23. *Bone* 2007, 40 (6): 1565-1573.
7. Kurosu H, Ogawa Y, Miyoshi M, Yamamoto M, Nandi A, Rosenblatt KP, Baum MG, Schiavi S, Hu MC, Moe OW *et al*: Regulation of Fibroblast Growth Factor-23 Signaling by Klotho. *The Journal of Biological Chemistry* 2006, 281 (10): 6120-6123.
8. Shimada T, Kakitani M, Yamazaki Y, Hasegawa H, Takeuchi Y, Fujita T, Fukumoto S, Tomizuka K, Yamashita T: Targeted ablation of *Fgf23* demonstrates an essential physiological role of FGF23 in phosphate and vitamin D metabolism. *The Journal of Clinical Investigation* 2004, 113 (4): 561-568.
9. Shalhoub V, Ward SC, Sun B, Stevens J, Renshaw L, Hawkins N, Richards WG: Fibroblast Growth Factor 23 (FGF23) and Alpha-Klotho Stimulate

- Osteoblastic MC3T3.E1 Cell Proliferation and Inhibit Mineralization. *Calcified Tissue International* 2011, 89 (2): 140-150.
10. Murali SK, Roschger P, Zeitz U, Klaushofer K, Andrukhova O, Erben RG: FGF23 Regulates Bone Mineralization in a 1,25(OH)₂D₃ and Klotho-Independent Manner. *Journal of Bone and Mineral Research* 2015. [Epub ahead of print]
 11. Chen CD, Podvin S, Gillespie E, Leeman SE, Abraham CR: Insulin stimulates the cleavage and release of the extracellular domain of Klotho by ADAM10 and ADAM17. *Proceedings of the National Academy of Sciences of the United States of America* 2007, 104 (50): 19796-19801.
 12. Xie J, Yoon J, An SW, Kuro-o M, Huang CL: Soluble Klotho Protects against Uremic Cardiomyopathy Independently of Fibroblast Growth Factor 23 and Phosphate. *Journal of the American Society of Nephrology* 2015, 26 (5): 1150-1160.
 13. Zhao Y, Banerjee S, Dey N, LeJeune WS, Sarkar PS, Brobey R, Rosenblatt KP, Tilton RG, Choudhary S: Klotho Depletion Contributes to Increased Inflammation in Kidney of the *db/db* Mouse Model of Diabetes via RelA (Serine)⁵³⁶ Phosphorylation. *Diabetes* 2011, 60 (7): 1907-1916.
 14. Tang X, Wang Y, Fan Z, Ji G, Wang M, Lin J, Huang S, Meltzer SJ: Klotho: a tumor suppressor and modulator of the Wnt/ β -catenin pathway in human hepatocellular carcinoma. *Laboratory Investigation* 2015. [Epub ahead of print]
 15. Nakatani T, Sarraj B, Ohnishi M, Densmore MJ, Taguchi T, Goetz R, Mohammadi M, Lanske B, Razzaque MS: *In vivo* genetic evidence for klotho-dependent, fibroblast growth factor 23 (Fgf23) -mediated regulation of systemic phosphate homeostasis. *FASEB journal* 2009, 23 (2): 433-441.
 16. Kawamoto T: Use of a new adhesive film for the preparation of multi-purpose fresh-frozen sections from hard tissues, whole-animals, insects and plants. *Archives of Histology and Cytology* 2003, 66 (2): 123-143.
 17. Lemaire R, Desmons A, Tabet JC, Day R, Salzet M, Fournier I: Direct Analysis and MALDI Imaging of Formalin-Fixed, Paraffin-Embedded Tissue Sections. *Journal of Proteome Research* 2007, 6 (4): 1295-1305.
 18. Ronci M, Bonanno E, Colantoni A, Pieroni L, Di Ilio C, Spagnoli LG, Federici

- G, Urbani A: Protein unlocking procedures of formalin-fixed paraffin-embedded tissues: Application to MALDI-TOF Imaging MS investigations. *Proteomics* 2008, 8 (18): 3702-3714.
19. Djidja MC, Claude E, Snel MF, Scriven P, Francese S, Carolan V, Clench MR: MALDI-Ion Mobility Separation-Mass Spectrometry Imaging of Glucose-Regulated Protein 78 kDa (Grp78) in Human Formalin-Fixed, Paraffin-Embedded Pancreatic Adenocarcinoma Tissue Sections. *Journal of Proteome Research* 2009, 8 (10): 4876-4884.
 20. Stauber J, MacAleese L, Franck J, Claude E, Snel M, Kaletas BK, Wiel IM, Wisztorski M, Fournier I, Heeren RM: On-Tissue Protein Identification and Imaging by MALDI-Ion Mobility Mass Spectrometry. *Journal of the American Society for Mass Spectrometry* 2010, 21 (3): 338-347.
 21. Cole LM, Mahmoud K, Haywood-Small S, Tozer GM, Smith DP, Clench MR: Recombinant " IMS TAG" proteins - A new method for validating bottom-up matrix-assisted laser desorption/ionisation ion mobility separation mass spectrometry imaging. *Rapid Communications in Mass Spectrometry* 2013, 27 (21): 2355-2362.
 22. Powers TW, Neely BA, Shao Y, Tang H, Troyer DA, Mehta AS, Haab BB, Drake RR: MALDI Imaging Mass Spectrometry Profiling of N-Glycans in Formalin-Fixed Paraffin Embedded Clinical Tissue Blocks and Tissue Microarrays. *PLoS One* 2014, 9 (9): e106255.
 23. Gravius S, Randau TM, Casadonte R, Kriegsmann M, Friedrich MJ, Kriegsmann J: Investigation of neutrophilic peptides in periprosthetic tissue by matrix-assisted laser desorption ionisation time-of-flight imaging mass spectrometry. *International orthopaedics* 2015, 39 (3): 559-567.
 24. O'Rourke MB, Djordjevic SP, Padula MP: A non-instrument-based method for the analysis of formalin-fixed paraffin-embedded human spinal cord via matrix-assisted laser desorption/ionisation imaging mass spectrometry. *Rapid Communications in Mass Spectrometry* 2015, 29 (19): 1836-1840.
 25. Fowler CB, O'Leary TJ, Mason JT: Toward improving the proteomic analysis of formalin-fixed, paraffin-embedded tissue. *Expert Review of Proteomics* 2013, 10 (4): 389-400.
 26. Prasad P, Donoghue M: A comparative study of various decalcification

- techniques. *Indian Journal of Dental Research* 2013, 24 (3): 302-308.
27. Athanasou NA, Quinn J, Heryet A, Woods CG, McGee JO: Effect of decalcification agents on immunoreactivity of cellular antigens. *Journal of Clinical Pathology* 1987, 40 (8): 874-878.
 28. Maran A, Gorny G, Oursler MJ, Zhang M, Shogren KL, Yaszemski MJ, Turner RT: 2-methoxyestradiol inhibits differentiation and is cytotoxic to osteoclasts. *Journal of Cellular Biochemistry* 2006, 99 (2): 425-434.
 29. Geng W, Hill K, Zerwekh JE, Kohler T, Muller R, Moe OW: Inhibition of Osteoclast Formation and Function by Bicarbonate: Role of Soluble Adenylyl Cyclase. *Journal of Cellular Physiology* 2009, 220 (2): 332-340.
 30. Suzuki H, Amizuka N, Oda K, Noda M, Ohshima H, Maeda T: Histological and elemental analyses of impaired bone mineralization in *klotho*-deficient mice. *Journal of Anatomy* 2008, 212 (3): 275-285.
 31. Liu R, Farach-Carson MC, Karin NJ: Effects of Sphingosine Derivatives on MC3T3-E1 Preosteoblasts: Psychosine Elicits Release of Calcium from Intracellular Stores. *Biochemical and Biophysical Research Communications* 1995, 214 (2): 676-684.
 32. Lyons JM, Karin NJ: A Role for G Protein-Coupled Lysophospholipid Receptors in Sphingolipid-Induced Ca²⁺ Signaling in MC3T3-E1 Osteoblastic Cells. *Journal of Bone and Mineral Research* 2001, 16 (11): 2035-2042.
 33. Kato K, Adachi S, Matsushima-Nishiwaki R, Minamitani C, Natsume H, Katagiri Y, Hirose Y, Mizutani J, Tokuda H, Kozawa O *et al*: Regulation by Heat Shock Protein 27 of Osteocalcin Synthesis in Osteoblasts. *Endocrinology* 2011, 152 (5): 1872-1882.
 34. Kim MK, Lee HY, Kwak JY, Park JI, Yun J, Bae YS: Sphingosine-1-phosphate stimulates rat primary chondrocyte proliferation. *Biochemical and Biophysical Research Communications* 2006, 345 (1): 67-73.
 35. Ishii M, Kikuta J: Sphingosine-1-phosphate signaling controlling osteoclasts and bone homeostasis. *Biochimica et Biophysica Acta* 2013, 1831 (1): 223-227.